

1 This is manuscript is a preprint and has been submitted to *Basin Research*. This manuscript
2 has undergone peer review. Subsequent versions of this manuscript may have different
3 content. If accepted, the final accepted version of this manuscript will be available via the
4 'Peer-reviewed Publication' DOI link on the right-hand side of this webpage. Please feel free
5 to contact any of the authors directly to comment on the manuscript. We welcome any
6 feedback!

7 Reflection Seismic Thermometry

8 *Arka Dyuti Sarkar*^{1,2}

9 *Mads Huuse*¹

10 ²Corresponding author: arkadyuti.sarkar@manchester.ac.uk

11 ¹Basins Research Group, Department of Earth and Environmental Sciences, University of
12 Manchester, Manchester M13 9PL, United Kingdom

13 Acknowledgement

14 This project was enabled by generous funding from Arka's parents, to whom the authors are
15 very grateful. Thanks go to CGG for provision of the North Viking Graben dataset and to
16 Schlumberger for provision of Petrel licenses (the software used for modelling). The authors
17 would like to thank Daniel Schmid, Christian Hardwick & Dave Muirhead for their comments
18 helping to refine and improve the manuscript. Special thanks go to Kofi Owusu for his
19 comments and assistance in modelling remotely during a pandemic. Thanks also go to
20 colleagues at the Basin Research Group for their support and guidance.

21 Abstract

22 The North Viking Graben (NVG) is part of the mature North Sea Basin petroleum province and
23 designated as a major carbon storage basin for NW Europe. It has been extensively drilled
24 over five decades with an abundance of well and seismic data in the public domain. As such
25 it serves as an excellent setting to demonstrate the efficacy of a reflection seismic data led
26 approach to predicting subsurface temperatures using a state-of-the-art full waveform
27 inversion velocity model covering the entire NVG. In a forward modelling approach, an
28 empirical velocity to thermal conductivity transform is used in conjunction with predefined

29 heatflow to predict subsurface temperature. The predefined heatflow parameters are set
30 based on the range of values from previous studies in the area. Abundant well data with
31 bottom hole temperature (BHT) records provide calibration of results. In the second step of
32 inverse modelling, BHT's as well as the velocity derived thermal conductivity are used to
33 evaluate a 1D steady state approximation of Fourier's Law for heatflow. In this way heatflow
34 is estimated over the 12000 km² model area at a km scale (lateral) resolution, highlighting
35 lateral variability in comparison to the traditional point-based heatflow datasets. This
36 heatflow is used to condition a final iterative loop of forward modelling to produce a
37 temperature model that is best representative of the subsurface temperature. Calibration
38 against 139 exploration wells indicate that the predicted temperatures are on average only
39 0.6 °C warmer than the recorded values, with a root mean squared error of 5 °C. BHT for the
40 recently completed Northern Lights carbon capture and sequestration (CCS) well 31/5-7 (Eos)
41 has been modelled to be 97 °C, which is 6 °C below the recorded BHT. This highlights the
42 applicability of this workflow not only towards enhancing petroleum systems modelling work
43 but also for use in the energy transition and for fundamental scientific purposes.

44 **Keywords:**

45 *Seismic; velocity modelling; subsurface temperature; heatflow*

46 **1. Introduction**

47 The importance of understanding the subsurface temperature conditions is manifold. An
48 understanding of the isotherms may help delineate important temperature driven diagenetic
49 boundaries (Bjørlykke et al., 1989). Similarly, it is useful for petroleum exploration as it
50 informs the maturity and types of hydrocarbons to be expected from a given source rock
51 (Allen & Allen, 2013). Unlike frontier areas where the effectiveness of source rocks may be in
52 doubt, this is not a concern in the North Sea. However, understanding of the present-day

53 subsurface temperature can still prove useful in such a mature basin. An example could
54 include identification of the so called “Golden Zone” thermal window in reservoirs (Nadeau,
55 2011). Similarly, an improved understanding of subsurface temperature could assist in
56 enhanced oil recovery (EOR) such as when CO₂ saturation is used to aid recovery of heavy oils
57 by reducing the density of the latter (Davarpanah & Mirshekari, 2020). Investigations into
58 geothermal energy also benefit from improved understanding of subsurface temperature
59 conditions (Bonté et al., 2012; Fuchs & Balling, 2016). The North Sea is one of the world’s
60 most prolific and extensively studied petroleum provinces (Copestake et al., 2003; Cornford,
61 1998; Leadholm et al., 1985; Rüpke et al., 2008). Over the course of the past sixty years
62 numerous oil and gas fields have been discovered, many of which have served as the testing
63 ground for new technologies such as time lapse 4D seismic or EOR (Awan et al., 2006; Landrø
64 et al., 1999). With this history of developing and applying cutting edge methodologies, it is a
65 fitting setting to test the workflow proposed here. This paper proposes and tests a means of
66 utilising reflection seismic data to predict subsurface temperatures. Previous work has
67 demonstrated that a transform based on empirical velocity and thermal conductivity data
68 may be utilised to convert seismic velocities to thermal conductivities (Sarkar, 2020; Sarkar &
69 Huuse, 2018). The derived thermal conductivities may be used in conjunction with heatflow
70 data, either from existing open-source data or through modelling of heatflow, to determine
71 subsurface temperatures from Fourier’s Law under a steady state condition. There have been
72 numerous studies of the thermal conductivities and heatflow of sediments in the northern
73 North Sea (Andrews-Speed et al., 1984; Brigaud et al., 1992; Cornelius, 1975; Evans, 1977;
74 Evans & Coleman, 1974; Houbolt & Wells, 1980; Leadholm et al., 1985). However, there seems
75 to be a hiatus in such studies in recent times. Projects such as the Northern Lights carbon

76 capture and sequestration (CCS) project (Cozier, 2019) would benefit greatly from current
77 knowledge of the subsurface thermal domain for full scale CCS.

78 *1.1 Thermal model fundamentals*

79 When considering heat in the shallow subsurface it is important to understand the sources of
80 heat. That the interior of the Earth is considerably hotter is known, with surface heatflow
81 distribution closely linked to the upper mantle (Pollack et al., 1993). However 40 % of outward
82 heatflow originates in the thin outer crust (Beardsmore & Cull, 2001). Primarily this crustal
83 heat generation is from the radioactive decay of unstable isotopes of elements such as
84 uranium, thorium and potassium (in order of heat production) (Mareschal & Jaupart, 2013).
85 This radioactive heat component is non uniform in the crust due to the variable distribution
86 of radioisotope bearing lithologies within the crust. Oceanic crust for example lacks acidic
87 rocks, which tend to have the highest radioactive heat production, and thus oceanic heatflow
88 has a lower internal heat component (Hasterok et al., 2011). To a lesser extent crustal heating
89 might arise from the frictional heating at faults or from metamorphic processes, which can be
90 either endo- or exothermic in nature (Beardsmore & Cull, 2001).

91 Fluid movement in the subsurface can lead to heatflow perturbations, particularly in young
92 oceanic crust (Lister, 1972). This might be mitigated by either having sufficient sediment cover
93 or distance from the nearest seamount (from where such hydrothermal fluid systems are
94 likely to originate) (Hasterok et al., 2011). Sediment cover and high rates of sedimentation
95 might also impact heatflow conditions in terms of sediment compaction and thermal rebound
96 with corresponding lower heatflow and suppressed thermal gradient seen in locations of high
97 sediment discharge such as the Bay of Bengal (Hasterok et al., 2011).

98 To understand how subsurface temperature might be modelled in the present day it is
99 important to establish the key thermal boundary conditions and properties. These are
100 heatflow, seabed temperature, thermal conductivity, the resultant geothermal gradient, and
101 subsurface temperature. The link between heatflow, thermal conductivity and geothermal
102 gradient can be represented by the 1D approximation of Fourier's Law (Eq. 1).

103 **Equation 1:** $q = k \times \frac{dT}{dZ}$

104 Where q is heatflow (mW m^{-2}); k is thermal conductivity ($\text{W m}^{-1} \text{K}^{-1}$) and dT/dZ is geothermal
105 gradient ($^{\circ}\text{C km}^{-1}$) where Z is positive downwards. To estimate the temperature at a certain
106 depth in the subsurface, the rate of change of temperature with depth, i.e. the geothermal
107 gradient is important. It becomes apparent then that by rearranging Eq. 1, the input
108 parameters necessary to estimate this are heatflow and thermal conductivity.

109 **Equation 2:** $\frac{dT}{dZ} = \frac{q}{k}$

110 Thermal conductivity is a measure of the ease with which heat may be conducted through a
111 material (Popov et al., 2003) and is thus critical to estimating the thermal structure of the
112 subsurface. Thermal conductivity data from direct measurements are made either in situ
113 through well logs or via direct measurements on recovered samples (Andrews-Speed et al.,
114 1984; Jorand et al., 2015; Schön, 2015a). Measuring tools include either a needle probe
115 inserted into a sample or a divided bar apparatus (Evans, 1977; Horai, 1982). However, these
116 measurements may suffer from issues that affect both their ease of acquisition and reliability.
117 For example thermal conductivity probes may have poor contact with borehole walls, or the
118 needle probe reading might be affected by the alignment of the mineral fabric (anisotropy) in
119 relation to the needle orientation (Lucazeau et al., 2004; Pribnow et al., 2000). In the case of
120 the divided bar apparatus, sample preparation is a more involved process, with the

121 application of axial load equivalent to hundreds of metres of overburden on samples having
122 the effect of increasing measurements on both dry and saturated samples (Galson et al.,
123 1987). A range of downhole measuring tools may be used to measure thermal conductivity
124 within the borehole however these are discontinuous measurements that are uneconomic
125 (Mielke et al., 2017). As a result there has been considerable thought put towards deriving
126 thermal conductivity from other more easily measured physical properties such as bulk
127 density, porosity or compressional sound wave velocity (Boulanouar et al., 2013; Esteban et
128 al., 2015; Grevenmeyer & Villinger, 2001; Gu et al., 2017; Hartmann et al., 2005; Horai, 1982;
129 Jorand et al., 2015). In the case of velocity, it is found to have similar sensitivity to properties
130 as thermal conductivity (Houbolt & Wells, 1980). That is, thermal conductivity is primarily
131 affected by the mineral composition, porosity and presence of fractures (Mielke et al., 2017;
132 Pimienta et al., 2018; Zamora et al., 1993). Temperature and pressure also impact thermal
133 conductivity though not as much as the other factors (Leadholm et al., 1985; Lee, 2003).

134 *Figure 1: Study area overview*

135 2. Geological history

136 The North Viking Graben (NVG) (Fig. 1) is located in the Northern North Sea between the East
137 Shetland Platform to the West and the Horda Platform to the east, and part of the north
138 western European cratonic block (Brigaud et al., 1992). It is part of the North Sea Graben
139 system (Fig. 2) (Cornford, 1998). It is a Mesozoic rift system, with the rifting in this area having
140 occurred after the Caledonian orogeny (and extensional orogenic collapse), with there being
141 two primary phases of extensional rifting since the Devonian (Fichler et al., 2011; Rüpke et
142 al., 2008; Ziegler, 1992). Primary rifting in the Permian to Early Triassic was followed by a post
143 rift subsidence period (Nøttvedt et al., 1995). The next phase of rifting was from mid Jurassic

144 to early Cretaceous and was also followed by a post rift subsidence period. The rift axis for
145 the Permo-Triassic rifting is believed to be located under the present Horda Platform with the
146 late Jurassic rift axis below the present day Viking Graben (Christiansson et al., 2000). No
147 major tectonic activity is believed to have occurred post Jurassic though there is some
148 conjecture regarding a Tertiary rifting episode (Rüpke et al., 2008) and mid Miocene inversion
149 (Løseth et al., 2013, 2016). The predominant rift direction in the N to NE striking Viking Graben
150 was west-east and northwest-southeast.

151 The sedimentary record in this area is Devonian and younger. Sand and shales dominate the
152 Triassic to Jurassic basin fill with carbonates and shales predominant in the Cretaceous
153 (Brigaud et al., 1992). Tertiary lithologies consist of shales, silts and sands, with a brief period
154 of Paleocene volcanism marked by the widespread deposition of volcanic tuffs across the
155 basin (Haaland et al., 2000). Crustal basement rocks in this area have a history exceeding one
156 Wilson cycle and trace back to the junction between the Laurentian and Baltican plates,
157 including the opening of the Iapetus Ocean, island arc development linked to oceanic
158 subduction and the Caledonian orogeny (Fossen et al., 2008; Meert & Torsvik, 2003). The
159 composition of the basement rocks can be seen to vary from granites underneath the East
160 Shetland Platform to low and intermediate grade metamorphic and metamorphosed
161 sediments below the Viking Graben and Horda Platform (Fichler et al., 2011).

162 Source rocks in the area are predominantly Kimmeridge Clay (shales) that were deposited in
163 the Late Jurassic (Davison & Underhill, 2012; Gautier, 2005). Abundant reservoir rocks are
164 available in the NVG all of which exist with a variety of trapping mechanisms. These pre rift
165 reservoirs are usually found in tilted fault blocks where fine-grained post rift sedimentary
166 sequences act as seals.

167 **Figure 2: Structural transect**

168 3. Data

169 The dataset used for the study includes reflection seismic and borehole data.

170 The North Viking Graben ‘mega-merge’ was acquired by CGG between 2014 and 2016,
171 covering a total area of 35410 km². This broadband 3D seismic reflection survey of BroadSeis™
172 and BroadSource™ configuration covers the northern North Sea basin and was shot in a north-
173 south direction, recorded in TWT down to 9 seconds with an acquisition sample interval of 2
174 ms (Purvis et al., 2018) though for this work the pre-stack depth migrated (PSDM) volume in
175 the depth domain was utilised. The volume has an inline and crossline bin spacing of 6.25 x
176 18.75 m. A (flip flop) shot point interval of 18.75 m and a source separation of 37.5 m gives a
177 nominal common-mid-point (CMP) fold of 106. Twelve streamers were used in total, each
178 7950 m long, with 636 channels towed at depths of 7 – 50 m (BroadSeis™ profile).

179 Multiple algorithms were used to remove noise and multiples. Both manual picking and time
180 tomographic inversion (TOMOT) was used to generate velocities with imaging done using
181 Kirchhoff PSTM. A proprietary CGG methodology of continuous automatic bi-spectral velocity
182 picking helped generate the final stacking velocities (Purvis et al., 2018). The processed PSTM
183 and PSDM cubes underpin the modelling work conducted in this study.

184 The full waveform inversion (FWI) technique aims to produce a high-fidelity subsurface
185 representation of velocity, as the velocity model minimises differences between observed
186 and modelled seismic waveforms within the original raw data (Warner et al., 2013). In making
187 the FWI velocity product, a best guess starting model based on seismic processing velocities
188 is iteratively improved using a sequence of linearized local inversions (Warner et al., 2013).
189 For the CGG NVG survey the fast track velocity product was made from the Dix conversion of
190 root mean squared (RMS) stacking velocities, followed by Kirchhoff depth migration to

191 residual move out (RMO) velocities (CGG, 2019). During the FWI process, the model was
192 subdivided into smaller areas targeting regions of key geology, allowing verification to be
193 conducted (CGG, 2019). Three production runs at ever increasing seismic frequency (4; 5.5 &
194 8 Hz) were conducted as part of the FWI model build (CGG, 2019). The final 8 Hz update
195 produced the velocity model that best follows geological structure and can characterise small
196 scale features such as injectites (CGG, 2019). The FWI model was calibrated using 101 wells
197 with QC checks completed against sonic log data (CGG, 2019).

198 Borehole data for this study were primarily sourced from the Norwegian Petroleum
199 Directorate (NPD) website. This gave access to well reports, mud logs, geological reports, and
200 wireline logging data. Because the FWI volume was already calibrated against downhole sonic
201 velocity data and provided in the depth domain, the primary data of interest for this study
202 were the corrected bottom hole temperatures (BHT) recorded for each well within the
203 thermal model area. Where drill stem test temperature readings are available these have
204 been used in the NPD dataset. Publicly available heatflow data from the International
205 Heatflow Commission (IHFC) database were used to provide constraint on the heatflow
206 parameter (Gosnold & Panda, 2002). There is a scarcity of data points covering the model
207 area as seen in Fig. 1b with the nearest offshore data point too distant to confidently
208 interpolate from (Ritter et al., 2004).

209 4. Methods

210 The modelling work has been conducted using Schlumberger's Petrel software used for 3D
211 seismic interpretation and to create and manipulate the property volumes and thermal
212 models in this work. Standard seismic interpretation techniques (Cox et al., 2020;
213 Posamentier, 2004), including horizon mapping, surface map creation and seismic attribute

214 extractions were conducted for a structural interpretation of two reference horizons, the
215 seafloor and the Base Cretaceous Unconformity (BCU). The BCU follows the regional
216 stratigraphic framework and serves as a reference horizon, upon which model outputs are
217 overlain as attributes, thus giving a regional context to the results (Evans, 2003). The seafloor
218 is the ceiling for the thermal models, separating the hydrothermal and the geothermal
219 domains. Both horizons were mapped in depth using the 3D reflection seismic data. For the
220 purposes of this work, no other structural interpretation was necessary. Further
221 interpretation or import of grids can of course be done to observe the predicted temperature
222 at desired stratigraphic levels.

223 The workflow utilised in this project is summarised in Fig. 3. It can be broken down into two
224 main components: the forward modelling approach uses the seismic velocity data as the input
225 parameter to model the thermal conductivity and subsurface temperature using constant
226 surface heatflows, which in turn is calibrated against available BHT data; the inverse approach
227 calculates heatflow from the observed BHTs and the thermal conductivity structure. As
228 heatflow is an important input parameter to model temperature, it becomes possible to
229 update the temperature forward model with the inverse modelling results, and thus validate
230 the final temperature model results, in a manner akin to tomographic update of velocity
231 models (Jones, 2018; Prada et al., 2019).

232 **Figure 3: Reflection seismic thermometry workflow**

233 *4.1 Forward modelling problem – present day subsurface temperature*

234 The reflection seismic dataset is a modern broadband seismic survey covering the North
235 Viking Graben (NVG) spanning across parts of the UK and Norwegian continental shelves
236 (UKCS and NCS, respectively). The full waveform inversion (FWI) final velocity model is the
237 key reflection seismic data product underpinning the modelling work.

238 *4.1.1 Thermal conductivity structure*

239 This study uses a high-resolution 3D seismic velocity volume and experimental data relating
240 velocity and conductivity with an empirical relationship (Fig. 4). As this project outlines a
241 remote sensing method, direct thermal conductivity measurement is not possible and instead
242 it must be indirectly determined. If the rocks of the subsurface are considered as a multi
243 component system comprised of minerals, texture (of grains, such as their shape and size),
244 porosity and the fluid content, it becomes possible in an ideal scenario to determine the
245 composite effective thermal conductivity from the contribution of each component part using
246 a suitable mixing law or effective medium model (Duffaut et al., 2018; Hartmann et al., 2005;
247 Schön, 2015b). Normally mud logging data (available here from the NPD database) would be
248 utilised to determine the volumetric fraction of each mineral (Brigaud et al., 1990). We,
249 however, are presenting a remote sensing scenario where only the temperature data from
250 wells is being used to correlate the predicted temperatures with.

251 The elastic properties of the subsurface are well constrained from seismic data (Mavko et al.,
252 2009) and it provides the avenue to the desired thermal structure. To link thermal properties
253 (thermal conductivity) to elastic properties (acoustic velocity), knowledge of their primary
254 controls becomes necessary. Experimental work has shown that these controls include
255 mineral composition, texture, porosity, the presence of fractures and fluid fill (Gegenhuber &

256 Schoen, 2012). It helps to think of porosity as the crucial intermediary in the proposed
257 empirical relationship as there have been studies examining the link between acoustic
258 velocity and porosity (Eberhart-Phillips et al., 1989; Lee, 2003; Velde, 1996); and similarly the
259 relationship between porosity and thermal conductivity (Fuchs & Förster, 2013; Jorand et al.,
260 2015). By making the direct leap it must be noted that there are inherent assumptions in such
261 an approach. One concern that may arise is the extent to which the variation in the velocity
262 signal solely corresponding to a thermal conductivity variation (as desired) or is it in fact
263 influenced by external factors (for example fluid overpressure). In such an instance, this issue
264 may be obviated by restricting application to regions of hydrostatic fluid pressure only,
265 however it might be the case that slight overpressure would only correspond to a minor
266 increase in velocity (Lee, 2003). While porosity is a crucial intermediary, mineral composition
267 has a dominant impact on thermal conductivity. Argillaceous rocks have lower conductivities
268 than non-argillaceous (quartz rich) rocks for example (Mavko et al., 2009). The more
269 monomineralic a rock, the greater the correlation between velocity and thermal conductivity
270 (Esteban et al., 2015), which alludes to the impact of anisotropy of thermal conductivity.
271 When considering clay rich rocks, they display poorer correlations for thermal conductivity
272 arising from the platy nature of clay grains (versus more rounded sand grains). At greater
273 compaction however, parallel alignment of clay grains could contribute towards lower
274 effective porosities and thus a stronger correlation with both velocity and thermal
275 conductivity (Velde, 1996). With use of this proposed empirical transform expected for both
276 shallow and deep intervals, it is hoped that the variability of clay rich sediment at shallow
277 levels is balanced at deeper levels.

278 It must be noted that even the best thermal conductivity models are subject to caveats, either
279 in the form of the inherent assumptions or the specific circumstances where direct
280 relationships might not be as strong.

281 By including a wide range of studies, covering a wide array of lithologies and settings, it is
282 hoped that the resulting empirical relationship can serve as a robust first order estimate for
283 the varying porosities encountered within any projected study area. Lithologies include clastic
284 sediments (sandstones of varying grain size from fine to coarse; varying mineral content
285 including nearly isotropic clean quartz rich sandstones & clay rich sandstones); carbonates
286 (limestone; dolomite; marl; etc); mudstones (clay- & siltstones); and volcanic & granitic rocks
287 (granite; basalt; gabbro; etc). The sample dataset is limited to wet samples only and
288 measurements taken using transient measurement apparatus such as the optical scanning
289 method (Popov et al., 1999), in order to maintain applicability to fluid filled rocks in the
290 subsurface and parity between data points respectively. Though the study area is dominated
291 by shales, the approach adopted with the empirical relationship is intended to be globally
292 applicable and thus incorporates samples not proportionally dominant in the NVG study. This
293 approach has previously been applied in passive margin settings offshore Namibia and
294 offshore USA (Sarkar & Huuse, 2018, 2021). Future studies could aim to utilise an edited
295 sample list reflective of the dominant lithologies in the target area. The best fit regression
296 (Fig. 4) through the subset of points is as follows:

297 **Equation 3:** $k_V = (6 \times 10^{-5})V_p^{1.3279}$

298 Where k_V is thermal conductivity from velocity ($\text{W m}^{-1} \text{K}^{-1}$) and V_p is P wave velocity (m s^{-1})

299 **Figure 4:** Empirical transform for velocity and thermal conductivity

300 With a highly detailed FWI velocity volume representing the P-wave velocity of the subsurface
301 and a function relating velocity and thermal conductivity, it is possible to convert the FWI
302 velocity volume into a volume of thermal conductivity varying with depth (using Eq. 3). To
303 facilitate the workflow the FWI interval velocity volume was first converted to an average
304 velocity volume in depth below the seabed (as the geotherm starts at seabed) and this in turn
305 allowed the estimation of instantaneous average thermal conductivity as a function of depth
306 in the entire volume.

307 *4.1.2 Heatflow input scenarios*

308 In order to determine the geothermal gradient (Eq. 2), information regarding the heatflow in
309 the study area is required alongside thermal conductivity.

310 A priori heatflow values were defined based on a combination of existing literature and data
311 from the IHFC. As seen on Fig. 1b, there is a paucity of IHFC data points in the study area. This
312 leads to examining the published record for maps of heatflow covering the North Sea, and
313 these tend to exist in the form of heatflow estimate grids at regional or global scale. Examining
314 these grids such as Davies (2013) or Lucazeau (2019), it becomes apparent that the heatflow
315 varies greatly at basin scale. This seems to depend not just on the size of the grid squares over
316 which the authors have applied their interpolation, but the exact technique used to
317 interpolate and the input parameters they have used will lead to this variability. Consequently
318 it was decided that analysis of the range of heatflow values that are observed in the literature
319 for this area (Andrews-Speed et al., 1984; Cornelius, 1975; Davies, 2013; Evans & Coleman,
320 1974; Harper, 1971; Leadholm et al., 1985; Lucazeau, 2019; Ritter et al., 2004) will be used to
321 define predetermined starting conditions for heatflow. By using the conclusions of these
322 existing studies, previous modelling accounting for factors such as the impact of the Curie

323 depth in the area or the impact of basal heatflow, is incorporated. This gives a low-, mid- and
324 high- case a priori surface heatflow of 60, 70 and 80 mW m⁻² respectively.

325 *4.1.3 Temperature grids & calibration*

326 Having determined thermal conductivity and established heatflow scenarios it becomes
327 possible to calculate three geothermal gradient scenarios for the model area. By convolving
328 this with the subsurface depth and incorporating the bottom water temperature (BWT) (i.e.,
329 seabed temperature) an estimate of present-day subsurface temperature can be made.

330 **Equation 4:** $T = T_{SEABED} + \left(\frac{dT}{dZ} \times Z_{SUBSURFACE}\right)$

331 where T is predicted temperature (°C); T_{SEABED} is the temperature at seabed (°C); dT/dZ is the
332 instantaneous geothermal gradient (°C km⁻¹) (Eq. 2); and $Z_{SUBSURFACE}$ is the subsurface depth
333 (km).

334 Early studies into the geothermal aspects of the North Sea would set temperature at the
335 seafloor to a constant, for example 10 °C (Cornelius, 1975; Evans & Coleman, 1974; Harper,
336 1971). Here however seafloor temperature was assigned through decadal averages from the
337 World Ocean Atlas (WOA) dataset (Boyer et al., 2014; Locarnini et al., 2013). Using the nearest
338 measurement node from the 0.25-degree grid of the WOA dataset, the temperature profile
339 (hydrothermal gradient) for this was used to interpolate seafloor temperatures across the
340 seafloor within the model area. Temperatures are found to be in the range of 6 to 9 °C with
341 seafloor temperatures in the shallower water of the UKCS averaging 7.3 °C, and in the
342 relatively deeper waters to the east, these temperatures average 8.7 °C. By basing the
343 seafloor temperatures on a decadal average, the variability of seasonal bottom water
344 conditions and longer scale variability will be negated. This gives a baseline temperature from

345 which the well readings can be seen in context to, particularly with regard to determining the
346 geothermal gradient.

347 Thermograms, or temperature profiles, depicting temperature change with depth are one
348 way of displaying the model results for each well site (Cornelius, 1975). Petrel allows for the
349 creation of synthetic logs from a reservoir model or pillar grid. This requires resampling the
350 temperature models into a pillar grid coincident with the extent of the area of interest. The
351 dimensions of the individual cells of the grid, and subsequently the total number of cells
352 constituting the entire grid are important with respect to the total compute power. The
353 modelling results displayed here have a lateral resolution of 50*50 m (XY orientation), with
354 the top of the model coinciding with mean sea level (MSL) and the base being set at 5.5 km
355 depth. It is important to establish the base for the thermal model as this will define the
356 interval over which geothermal gradient is calculated. This basal depth encompasses the
357 maximum vertical depth of the wells used for calibration. Cell height was set to 20 m, in
358 accordance with the vertical resolution of the velocity data. For these dimensions, the entire
359 gridded model comprises about 1.4 billion voxels.

360 With all the input and derived seismic attributes resampled as properties in the pillar grid,
361 synthetic logs for each well are generated. These synthetic logs are made for the three
362 temperature prediction volumes coincident with the three heatflow input scenarios. The
363 estimated temperature at the bottom of each well from the synthetic logs is then plotted
364 against the recorded corrected BHT (Fig. 7). Theoretically, the misfit between observed and
365 modelled temperature for each well can be used to calculate how much the heatflow input
366 for each well must be adjusted for there to be no misfit. In this way, the most representative
367 heatflow value for the area might be calibrated.

4.2 Inverse modelling problem – solving for heatflow

368

369 The first stage of subsurface temperature modelling assumed 3 discrete heatflow parameter
370 input scenarios. In this instance, discrete values for heatflow across the model area were used
371 to simulate each temperature scenario. However, heatflow is likely not homogeneous across
372 the model area and there may be lateral variability across individual structures and preferred
373 fluid migration paths. If recorded temperatures in the wells are assumed to be correct and
374 with knowledge of the seafloor temperature, geothermal gradient can be independently
375 computed for each well site. Additionally, if the seismic velocity derived thermal conductivity
376 is considered valid, it becomes possible to use the 1D approximation of Fourier's Law to derive
377 heatflow at each well location. This is the inverse problem.

378 **Equation 5:** $q = K_V \times \left(\frac{T_{BHT} - T_{SEAFLOOR}}{dZ} \right)$

379 Where q is heatflow (mW m^{-2}); K_V is thermal conductivity from velocity ($\text{W m}^{-1} \text{K}^{-1}$); T_{BHT} is
380 bottom hole temperature ($^{\circ}\text{C}$); $T_{SEAFLOOR}$ is temperature at seafloor ($^{\circ}\text{C}$); and dZ is the vertical
381 depth interval (km).

382 Interpolating for heatflow between the wells creates a map of inversely modelled laterally
383 varying heatflow. An inverse distance weighting (IDW) function has been used to interpolate
384 heatflow. The values of cells in the vicinity of the processing cell (interpolated gap) are
385 averaged, with the distance of the neighbouring cell having an inverse weighting (Watson &
386 Philip, 1985).

387

4.3 Final temperature model

388 Calibrating the results of the temperature forward model with the different heatflow input
389 scenarios, it is likely to show different degrees of agreement. Iteratively updating the heatflow

390 parameter input each time and remodelling for subsurface temperature should theoretically
391 permit the most representative heatflow across the study area to be arrived at ultimately.
392 However, this former approach was not pursued as it was shown previously that inverse
393 modelling (see section 4.2) allows the determination of laterally varying heatflow across the
394 model area. Convolving this heatflow with the seismically derived thermal conductivity (Eq.
395 2), it should be possible to generate a volume of instantaneous geothermal gradient that has
396 most agreement across all the calibration wells. This thermal gradient is used to generate a
397 final temperature model (Eq. 4) that is resampled into the pillar grid and used to output
398 synthetic temperature logs. Predicted temperature from these logs at hole bottom is
399 extracted and used to calibrate against recorded BHT as before.

400 The well 31/5-7 is located due southwest of Troll A field and targets the lower Jurassic Cook
401 and Johanssen formations for injection. The targeted interval has ca.173 m of sandstone
402 overlain by 75 m of shale acting as a seal above it. Pressure data indicates no communication
403 in rocks above and below the shale, reinforcing its seal properties. With no results from this
404 well published due to its very recent completion, it was decided to use the available details
405 (well head coordinates and total depth) to simulate the temperature profile for this well using
406 our model.

407 5. Results

408 The results from the modelling work are presented either as seismic attribute overlays on
409 transects or by means of attribute maps on a gridded horizon. But for the purposes of
410 calibration the primary output is the synthetic temperature log data from the wells. These
411 results are discussed individually in the following section.

412 The FWI interval velocity volume was converted to an average velocity volume, before
413 applying the velocity to thermal conductivity transform (Fig. 4) to produce a volume of
414 average thermal conductivity. Looking at the internal velocity derived thermal conductivity
415 structure (Fig. 5b), the direct nature of the bulk shift results in the thermal conductivity
416 variation with depth across the volume corresponding to the level of detail seen in the input
417 velocity (Fig. 5a). Cretaceous and younger Cenozoic sediment cover is seen to have relatively
418 low thermal conductivities, with a distinct increase in thermal conductivity seen in the tilted
419 fault blocks of the Viking Graben. The graben corresponds with the greatest amount of
420 overlying sediment cover and lower conductivities relative to the neighbouring rift shoulder.

421 **Figure 5: Derived thermal conductivity structure**

422 The forward modelling results using the predefined heatflow input scenarios are displayed on
423 the west-east transect A-A' (see Fig. 6). As expected, temperatures increase gradually with
424 depth, with no major anomalous zones seen. Cenozoic sediments are coolest with the highest
425 temperatures in the graben itself, which makes sense considering constant heatflow but
426 lower conductivities of the sediments within the graben. Isotherms are more widely spaced
427 as we move towards the Horda Platform in the east where the conductivity is greater. As
428 predicted by Fourier's Law, increasing heatflow leads to increased subsurface temperatures.
429 The direct impact of each heatflow input scenario is better visualised when cross plotting the
430 temperature extracted from each well (Fig. 7).

431 **Figure 6: Forward modelling output for heatflow scenarios**

432 As stated earlier, synthetic thermograms corresponding to the well path of each calibration
433 well were extracted from the predicted temperature models. The temperature at bottom
434 hole in each case has been plotted against the recorded BHT. The best fit regression through
435 each cluster of points and the gradient of this is used as a measure of the degree of agreement

436 between predicted and observed values. The R-squared value, a measure of statistical validity
437 for each regression line, for all three heatflow scenarios is above the 0.7 that is regarded as
438 being the threshold for statistical reliability. Analysing the misfit between predicted BHT and
439 corrected BHT, it is found that on average the low heatflow scenario is 0.64 °C cooler; the mid
440 heatflow scenario has average misfit 15.4 °C higher and the high heatflow scenario has an
441 average misfit of 31.3 °C higher. With increasing heatflow, the corresponding gradient of the
442 regression line through that cluster of points also increases, as does the Y-intercept. The
443 optimum desired gradient that would be expected for best agreement between predicted
444 and observed temperatures would verge on 1, and from this initial forward modelling it is
445 seen that the lowest heatflow scenario is closest to this. However, it is also the case that the
446 optimum regression should be seen to pass through the origin of the cross plot and increasing
447 the heatflow moves each regression further away from this.

448 **Figure 7: Forward modelling results calibrated**

449 When deriving ocean bottom heatflow across the model area through an inverse modelling
450 problem (see 4.2) (Fig. 8), gives mean heatflow of 60.05 mW m⁻² and a median of 62.82 mW
451 m⁻². The effective range of heatflow is between 40 to 70 mW m⁻². Observing the heatflow
452 variation across the area (Fig 8) certain wells are seen to have much lower heatflow than their
453 immediate vicinity. Consequently, during interpolation, these wells are seen in a bulls-eye
454 zone of depressed heatflow. The most prominent of these is observed to the southwest, with
455 two wells (30/5-1 & 30/8-2) having depressed effective heatflow. Referring to Fig. 1 these two
456 wells do not coincide with any field. The other prominent heatflow depression is found to the
457 northeast of the model area at the intersection between Troll-A and Troll-B. The north-
458 westernmost and easternmost wells (29/3-1 & 32/4-1, respectively) (Fig. 8) influence the
459 immediate vicinity by elevating the heatflow interpolated here.

460 **Figure 8: Inverse modelling of heatflow and results**

461 The result of running a final iteration of forward modelling for temperature with the
462 continually laterally varying heatflow derived in Fig. 8 is shown in Fig. 9. We find when cross
463 plotting predicted temperatures from this final model against BHT that the general
464 distribution of points has a far tighter spread than in the previous modelling instances. The
465 average misfit between predicted BHT and measured BHT is 0.58 °C. Furthermore, the best
466 fit regression through this set of points has a gradient nearly equal to 1, and passes nearest
467 to the origin, as is expected for the model best reflecting the actual subsurface temperature.
468 Interestingly, the average of the inverse modelled heatflow as stated earlier is nearly equal
469 to the low case heatflow input scenario used in the early-stage forward modelling. Looking at
470 the distribution of well points (Fig. 9) however it is clear that there is a great disparity in the
471 two approaches. The visual impact of the two approaches is shown in Fig. 10d, e.

472 **Figure 9: Well calibration including final temperature model**

473 The result from the final iteration of the temperature model overlain with key structures is
474 shown in Fig. 10a. Running an RMS amplitude extraction for thermal conductivity on a
475 reference horizon (Fig. 10c), in this case the BCU, it is observed that the highest thermal
476 conductivities are observed in the heart of the Viking Graben, where the BCU is deepest (Fig.
477 10b). On the flanks of the graben and eastward towards the Horda Platform, thermal
478 conductivities are seen to decrease considerably, consistent with the increasingly shallowing
479 BCU surface at that point. Reverting to the temperature model outputs, we see the difference
480 between the initial forward modelling approach (Fig. 10d) and the final inverse modelled
481 heatflow influenced iteration (Fig. 10e). Comparing the temperatures, within the deep graben
482 for example, it is immediately apparent there is greater variation and detail discernible in
483 from this latter approach. Indeed, what is seen is that some anomalous temperature zones

484 are seen in this final iteration at the northern tip of the Troll field that seem to directly
485 correlate with the anomalous heatflow zone from the interpolation (see Fig. 8a).

486 **Figure 10: Temperature modelling results**

487 The results of simulating the thermal profile for the Northern Lights well 31/5-7 (Eos) are
488 shown in Fig. 11, with temperature at bottom hole of 97 °C falling well within the projected
489 100 °C range published on the project website (see: <https://northernlightscs.com/en/about>
490 accessed at 25/07/2020). Data released by Equinor and the Norwegian government in
491 October 2020 with preliminary results indicated temperature at the bottom of 103 °C. The
492 final well report with its BHT record has not yet been made public but preliminary results from
493 the 31/5-7 prediction show a good agreement between model prediction and reality.

494 **Figure 11: CCS well 31/5-7 modelled**

495 **6. Discussion**

496 There are multiple corollaries of modelling for subsurface temperature in this manner. The
497 seismic led method of deriving subsurface thermal conductivity structure should enable the
498 verification of zones of thermal blanketing (Cercione & Pollack, 1991; Wangen, 1995). Due to
499 the direct relationship between velocity and thermal conductivity as used here, any zones of
500 anomalously high or low velocity will be reflected in thermal conductivity anomalies. The
501 general trend contains lithologies such as sandstone, shale, limestone and crystalline rocks.
502 This excludes lithologies that deviate from our general trend such as halite, which will need
503 to be considered explicitly to represent the temperature above, within and below such
504 anomalous bodies.

505 The benefit of the highly detailed FWI velocity model available in this area is that the velocity
506 data has been calibrated against wells in the NVG, thus ensuring the velocity model is a good

507 representation of true subsurface properties and conditions. The conversion to thermal
508 conductivity and temperature provides another means of visualising the subsurface. It is of
509 critical importance to both petroleum exploration and carbon sequestration in the area. In
510 other locations such estimates would be highly beneficial to geothermal or gas storage
511 operations. It must be noted that any artefacts in the velocity data will be translated to the
512 derived thermal conductivity, instantaneous geothermal gradient and predicted temperature
513 volumes as a consequence of the direct transitions in the workflow.

514 *6.1 Heatflow modelling – impact and implications*

515 The validation of the inverse modelling of heatflow as an input as opposed to the use of a
516 discrete integer value heatflow input is borne out by the results. The interpolation of heatflow
517 over the 12000 km² model area (Fig. 8) highlights the variation in heatflow magnitude laterally
518 at improved coverage compared to most existing studies. As shown earlier (Fig. 1), global and
519 regional compilations usually produce heatflow grids that are at the scale of 1-degree grid
520 squares or larger. The lateral resolution is thus many orders of magnitude poorer than when
521 based on BHT and conductivity data. Interpolating heatflow at such fine scale might enable
522 the examination of any trends, if any, in heatflow versus features that may be hydrocarbon
523 fields, or structural trends (for example major fault networks). While there is a paucity of data
524 points in the IHFC grid coinciding with large parts of the Northern and Central North Sea, the
525 many decades of hydrocarbon exploration in the area led to numerous wells, many of which
526 have detailed records of BHT. When combined with the seismic velocity driven model to
527 ascertain thermal conductivity structure, it should allow for the possibility to fill in the large
528 gaps in the global point heatflow database, which in turn should allow for more detailed basin
529 scale heatflow studies.

530 The thermal anomaly visible in the interpolated ocean bottom surface heatflow map (Fig. 8)
531 can be seen to coincide with the Troll Field (Fig. 1). Records of this thermal anomaly attribute
532 it to transient effects of uplift caused by late Quaternary deglaciation (Cornford, 1998). The
533 method used to interpolate heatflow might have an impact. IDW gives the best results when
534 the sampling is sufficiently dense with respect to the local variation being simulated (Watson
535 & Philip, 1985). Where sampling is sparse or uneven, the interpolated result will insufficiently
536 represent the desired surface (Philip & Watson, 1982). From the density of wells around
537 existing fields in the area, we can be sure that the IDW interpolation will reliably capture the
538 laterally varying heatflow at this local scale. Nonetheless at the edges of the model area there
539 will be some degree of uncertainty associated with the interpolated heatflow, a consequence
540 of the sampling sparseness in these regions. Kriging would be a more statistically rigorous
541 method of interpolating heatflow, but it requires a prior investigation of the spatial behaviour
542 of heatflow in the sample points. This is incumbent on a pre-existing understanding of the
543 factors influencing the modelled parameter. In a blind test the latter would not necessarily be
544 possible, and thus IDW should be satisfactory for a first order interpretation.

545 While heatflow has been derived from inverse modelling, in sedimentary basins there is a
546 thermal contribution linked to the radiogenic heat production of sediments and crustal
547 material, and the contribution of heat from the earth's deep interior (that is mantle) (Allen &
548 Allen, 2013; Hasterok et al., 2011; Hasterok, 2010; Hokstad et al., 2017). The modelling here
549 estimated present-day subsurface temperatures using a steady state approximation (Eq. 1).
550 As such, a conscious decision was made to introduce as few variables as possible. Radiogenic
551 heat production would be one such variable. Its impact here has been noted but not explicitly
552 modelled. Mantle heat production is usually estimated from the Moho, whose depth in the
553 area averages roughly 30 km (Grad & Tiira, 2009). Estimates of the Curie isotherm at its

554 shallowest in the study area place it at similar average depths of ca.30 km (Fichler et al., 2011;
555 Kubala et al., 2003). Under the graben, Moho depth does become shallow, up to 22 km in
556 places (Licciardi et al., 2020). Referring to Fig. 8a, modelled heatflow is higher towards the
557 graben centre, which suggests some correlation. With the thermal model base set at 5.5 km,
558 and the degree of shallowing of the Moho not exceeding ~22 km at its shallowest point, the
559 impact of mantle heat input from a modelling perspective is considered negligible in this
560 instance. The general Moho trend in the northern North Sea has a gradual shallowing in the
561 north-west, near the Shetland Islands (Licciardi et al., 2020). If conducting thermal modelling
562 over the whole NVG survey area, and with the basal limits for the model set sufficiently deep
563 such that there might be a basal mantle heatflow effect due to proximity to the Moho for the
564 deepest section of the model. Future models seeking to integrate surface heatflow with a
565 basal heatflow flux can rely on the Curie depth for constraint (Blakely, 1988). The Curie depth
566 is often seen to coincide with a compositional boundary reflecting the loss of magnetic
567 minerals in rocks (Rajaram et al., 2009) and thus can be treated as an isotherm, identifiable
568 using magnetic geophysical methods. It should become possible then to contrast modelled
569 surface heatflow against calculated surface heatflow from past studies, allowing
570 determination of whether the sensitivity of NVG thermal anomalies is to basal flux or thermal
571 conductivity effects, or a combination of the two factors.

572 *6.2 Relevance*

573 The applications of this proposed workflow range from immediate usage by the hydrocarbon
574 industry to supporting new subsurface uses aligned with the energy transition. Hydrocarbon
575 explorationists may use the knowledge of the isotherms to help develop their petroleum
576 systems models or it can help production teams better ascertain the distribution of

577 temperature in the reservoir in order to inform reservoir engineering projects to maximise
578 recovery. Knowledge of subsurface thermal structure is important for the nuclear waste
579 disposal industry due to the sensitivity of the waste to thermal perturbations (Brigaud et al.,
580 1992). From a low carbon technology solutions perspective, mapping subsurface isotherms
581 may enable geothermal energy prospecting and the understanding of subsurface
582 temperature will be important for CCS operations in both frontier and mature basins.

583 Simulating temperatures for the current CCS Northern Lights well 31/5-7 emphasises the real-
584 world applicability of this model, both in terms of its speed of producing an estimate and its
585 relevance in the energy transition for the future. It is important to understand the
586 temperature conditions in CO₂ storage reservoirs as the properties of the gas vary with
587 temperature and pressure. Of these only the pressure is routinely estimated based on seismic
588 data (Eiken et al., 2011). At higher temperatures the density of CO₂ decreases, theoretically
589 allowing for a greater volume of it to be stored in a reservoir. Studies of CO₂ injection into the
590 Utsira formation (part of the Sleipner Project) have shown that reservoir temperature is a
591 source of uncertainty as it can also impact the diffusivity of the gas within the reservoir
592 (Chadwick et al., 2006). By using the subsurface thermal model proposed here, this key
593 uncertainty may be constrained by project planners, both giving more constraint on the
594 volume of CO₂ able to be sequestered within a reservoir, but also the ability to ascertain
595 lateral temperature variability would enable more nuanced storage across different parts of
596 a reservoir. Finally understanding the temperature conditions and where the potential of CO₂
597 diffusivity is highest could help mitigate the possibility of CO₂ leakage.

598 It is not just industrial applications for which this methodology may be utilised. Academic end
599 use cases are also envisioned. The study of the microorganisms endemic to the deep
600 subsurface is nascent and opens up the possibility of the crust playing host to potentially great

601 biodiversity and biomass (Basso et al., 2005). Limited studies into the microbial organisms
602 found in oil reservoirs have yielded surprising results. One such study in the Troll field,
603 examining the microbial diversity of produced water, indicated that these microbes were not
604 introduced as contaminants into the reservoir as a by-product of drilling; instead RNA
605 analyses and gene matching has indicated that these are a distinct genera of temperature
606 sensitive microbes that do not match existing known mesophiles or thermophiles (Dahle et
607 al., 2008). Due to the temperature dependence of these novel microbes, and the difficulty
608 with sampling, an understanding of subsurface conditions might help in providing some
609 inclination of the exact genera that can be encountered in a reservoir based on the predicted
610 temperatures from the model. Thus, it is envisioned that the proposed model can assist the
611 microbiological community as well. Bacterial remediation has been studied as a means of
612 clean up for chemical or hydrocarbon contaminated reservoirs or aquifers (Hazen, 1997).
613 Understanding of the temperature field in the subsurface can help determine how conducive
614 the conditions are to the proliferation of such organisms. From a resource perspective
615 microorganisms have been found to impact natural gas, carbon sequestration, hydrocarbons
616 or even interfere with the underground storage of nuclear waste (Christofi & Philip, 1997).

617 7. Conclusion

618 The work outlines a novel methodology that utilises state of the art velocity model data from
619 a mature basin such as the North Viking Graben to determine present day subsurface
620 temperatures non-invasively. Forward modelling simulations underpinned by the velocity
621 data and utilising an empirical thermal conductivity transform have been calibrated against
622 recorded temperature data from oil field wells in this sector of the North Sea. Existing work
623 using well data allows the computing of the vertical component of heatflow, in the same

624 orientation as the well. Through inverse modelling here it has been demonstrated that
625 heatflow can be computed in such a manner that lateral heatflow variability coverage is
626 improved compared to existing datasets. Using this derived heatflow to iteratively update the
627 forward model produced a temperature model, the calibration results for which indicate the
628 validity of this approach. To prove the real-world efficacy of this work it has been applied to
629 a recently drilled carbon capture and sequestration well, estimating the temperature in the
630 target reservoir to be within a 5 °C margin at ~3 km subsurface depth, highlighting the
631 usability and robustness of this methodology in hydrocarbon exploration and future energy
632 transition projects.

633 8. References

- 634 Allen, P., & Allen, J. (2013). Basin analysis: principles and application to petroleum play
635 assessment. In *WileyBlackwell*.
- 636 Andrews-Speed, C. P., Oxburgh, E. R., & Cooper, B. A. (1984). Temperatures and Depth-
637 Dependent Heat Flow in Western North Sea. *American Association of Petroleum*
638 *Geologists Bulletin*, 68(11), 1764–1781.
- 639 Awan, A. R., Teigland, R., & Kleppe, J. (2006). EOR survey in the North Sea. *Proceedings - SPE*
640 *Symposium on Improved Oil Recovery*, 1, 294–309. <https://doi.org/10.2523/99546-ms>
- 641 Basso, O., Lascourrèges, J., Jarry, M., & Magot, M. (2005). The effect of cleaning and
642 disinfecting the sampling well on the microbial communities of deep subsurface water
643 samples. *Environmental Microbiology*, 7(1), 13–21. [https://doi.org/10.1111/j.1462-](https://doi.org/10.1111/j.1462-2920.2004.00660.x)
644 [2920.2004.00660.x](https://doi.org/10.1111/j.1462-2920.2004.00660.x)
- 645 Beardsmore, G., & Cull, J. (2001). Crustal Heat Flow: A Guide to Measurement and Modelling.
646 In *Cambridge University Press*. <https://doi.org/10.1017/S0016756803218021>
- 647 Becker, J. J., Sandwell, D. T., Smith, W. H. F., Braud, J., Binder, B., Depner, J., Fabre, D., Factor,
648 J., Ingalls, S., Kim, S.-H., Ladner, R., Marks, K., Nelson, S., Pharaoh, A., Trimmer, R., Von
649 Rosenberg, J., Wallace, G., & Weatherall, P. (2009). Global Bathymetry and Elevation
650 Data at 30 Arc Seconds Resolution: SRTM30_PLUS. *Marine Geodesy*, 32(4), 355–371.
651 <https://doi.org/10.1080/01490410903297766>
- 652 Bjørlykke, K., Ramm, M., & Saigal, G. C. (1989). Sandstone diagenesis and porosity
653 modification during basin evolution. *Geologische Rundschau*, 78(1), 243–268.
654 <https://doi.org/10.1007/BF01988363>
- 655 Blakely, R. J. (1988). Curie temperature isotherm analysis and tectonic implications of
656 aeromagnetic data from Nevada. *Journal of Geophysical Research*, 93(B10), 11817–

- 657 11832. <https://doi.org/10.1029/JB093iB10p11817>
- 658 Bonté, D., Van Wees, J. D., & Verweij, J. M. (2012). Subsurface temperature of the onshore
659 Netherlands: New temperature dataset and modelling. *Geologie En*
660 *Mijnbouw/Netherlands Journal of Geosciences*, 91(4), 491–515.
661 <https://doi.org/10.1017/S0016774600000354>
- 662 Boulanouar, A., Rahmouni, A., Boukalouch, M., Samaouali, A., Géraud, Y., Harnafi, M., &
663 Sebbani, J. (2013). Determination of Thermal Conductivity and Porosity of Building Stone
664 from Ultrasonic Velocity Measurements. *Geomaterials*, 03(04), 138–144.
665 <https://doi.org/10.4236/gm.2013.34018>
- 666 Boyer, T. P., Garcia, H. E., Locarnini, R. A., Zweng, M. M., Mishonov, A. V., Reagan, J. R.,
667 Antonov, J. I., Baranova, O. K., Biddle, M. M., Johnson, D. R., & Paver, C. R. (2014). 2013
668 World Ocean Atlas Aids High-Resolution Climate Studies. *Eos, Transactions American*
669 *Geophysical Union*, 95(41), 369–370. <https://doi.org/10.1002/2014EO410002>
- 670 Brigaud, F., Chapman, D. S., & Le Douaran, S. (1990). Estimating thermal conductivity in
671 sedimentary basins using lithologic data and geophysical well logs. *American Association*
672 *of Petroleum Geologists Bulletin*, 74(9), 1459–1477. [https://doi.org/10.1306/0C9B2501-](https://doi.org/10.1306/0C9B2501-1710-11D7-8645000102C1865D)
673 [1710-11D7-8645000102C1865D](https://doi.org/10.1306/0C9B2501-1710-11D7-8645000102C1865D)
- 674 Brigaud, F., Vasseur, G., & Caillet, G. (1992). Thermal state in the north Viking Graben (North
675 Sea) determined from oil exploration well data. *Geophysics*, 57(1), 69–88.
676 <https://doi.org/10.1190/1.1443190>
- 677 Cercone, K. R., & Pollack, H. N. (1991). Thermal maturity of the Michigan Basin. *Special Paper*
678 *of the Geological Society of America*, 256, 1–12. <https://doi.org/10.1130/SPE256-p1>
- 679 CGG. (2019). *Final Report, CGG18M01:Horda/Tampen PSDM, Offshore Norway - North Viking*
680 *Graben (NVG)*.
- 681 Chadwick, A., Arts, R., Eiken, O., Williamson, P., & Williams, G. (2006). Geophysical Monitoring
682 of the CO2 plume at Sleipnir, North Sea. *Nato Science Series: IV: Earth and Environmental*
683 *Sciences*, 65(Advances in the Geological Storage of Carbon Dioxide), 303–314.
684 https://doi.org/10.1007/1-4020-4471-2_25
- 685 Christiansson, P., Faleide, J. I., & Berge, A. M. (2000). Crustal structure in the northern North
686 Sea: An integrated geophysical study. *Geological Society Special Publication*,
687 167(McKenzie 1978), 15–40. <https://doi.org/10.1144/GSL.SP.2000.167.01.02>
- 688 Christofi, N., & Philip, J. C. (1997). European Microbiology Related to the Subsurface Disposal
689 of Nuclear Waste. In P. S. Amy & D. L. Haldeman (Eds.), *Microbiology of the Terrestrial*
690 *Deep Subsurface* (pp. 267–268). CRC Press.
- 691 Copestake, P., Sims, A., Crittenden, S., Hamar, G., Ineson, J., & Bathurst, P. (2003). The
692 Millennium Atlas : Petroleum Geology of the Central and Northern North Sea. In D.
693 Evans, C. Graham, A. Armour, & P. Bathurst (Eds.), *Geological Society of London*.
694 Geological Society of London.
695 <https://doi.org/https://doi.org/10.1017/S0016756803218124>
- 696 Cornelius, C. D. (1975). Geothermal aspects of hydrocarbon exploration in the North Sea Area.
697 *Norges Geologiske Undersøkelse Bulletin*, 316, 29–67.

- 698 Cornford, C. (1998). Source Rocks and Hydrocarbons of the North Sea. In K. W. Glennie (Ed.),
699 *Petroleum Geology of the North Sea* (pp. 376–462). Blackwell Science Ltd.
700 <https://doi.org/10.1002/9781444313413.ch11>
- 701 Cox, D. R., Newton, A. M. W., & Huuse, M. (2020). An introduction to seismic reflection data:
702 acquisition, processing and interpretation. In N. Scarselli, J. Adam, & D. Chiarella (Eds.),
703 *Regional geology and tectonics: principles of geologic analysis* (pp. 571–603). Elsevier.
- 704 Cozier, M. (2019). CCS takes centre stage. *Greenhouse Gases: Science and Technology*, 9(6),
705 1084–1086. <https://doi.org/10.1002/ghg.1942>
- 706 Crameri, F., Shephard, G. E., & Heron, P. J. (2020). The misuse of colour in science
707 communication. *Nature Communications*, 11(1), 5444. [https://doi.org/10.1038/s41467-](https://doi.org/10.1038/s41467-020-19160-7)
708 [020-19160-7](https://doi.org/10.1038/s41467-020-19160-7)
- 709 Dahle, H., Garshol, F., Madsen, M., & Birkeland, N.-K. (2008). Microbial community structure
710 analysis of produced water from a high-temperature North Sea oil-field. *Antonie Van*
711 *Leeuwenhoek*, 93(1–2), 37–49. <https://doi.org/10.1007/s10482-007-9177-z>
- 712 Davies, J. H. (2013). Global map of solid Earth surface heat flow. *Geochemistry, Geophysics,*
713 *Geosystems*, 14(10), 4608–4622. <https://doi.org/10.1002/ggge.20271>
- 714 Davison, I., & Underhill, J. R. (2012). Tectonics and Sedimentation in Extensional Rifts. In D.
715 Gao (Ed.), *Tectonics and Sedimentation* (pp. 15–42). American Association of Petroleum
716 Geologists. <https://doi.org/10.1306/13351547M1001556>
- 717 Duffaut, K., Hokstad, K., Kyrkjeb, R., & Wiik, T. (2018). A simple relationship between thermal
718 conductivity and seismic interval velocity. *Leading Edge*, 37(5), 381–385.
719 <https://doi.org/10.1190/tle37050381.1>
- 720 Eberhart-Phillips, D., Han, D. H., & Zoback, M. D. (1989). Empirical relationships among seismic
721 velocity, effective pressure, porosity, and clay content in sandstone. *Geophysics*, 54(1),
722 82–89. <https://doi.org/10.1190/1.1442580>
- 723 Eiken, O., Ringrose, P., Hermanrud, C., Nazarian, B., Torp, T. A., & Høier, L. (2011). Lessons
724 Learned from 14 years of CCS Operations: Sleipner, In Salah and Snøhvit. *Energy*
725 *Procedia*, 4, 5541–5548. <https://doi.org/10.1016/j.egypro.2011.02.541>
- 726 Esteban, L., Pimienta, L., Sarout, J., Piane, C. D., Haffen, S., Geraud, Y., & Timms, N. E. (2015).
727 Study cases of thermal conductivity prediction from P-wave velocity and porosity.
728 *Geothermics*, 53, 255–269. <https://doi.org/10.1016/j.geothermics.2014.06.003>
- 729 Evans, T. R. (1977). Thermal Properties of North Sea Rocks. *Log Analyst*, 18(2), 3–12.
- 730 Evans, T. R., & Coleman, N. C. (1974). North Sea geothermal gradients. *Nature*, 247(5435), 28–
731 30. <https://doi.org/10.1038/247028a0>
- 732 Færseth, R. B. (1996). Interaction of Permo-Triassic and Jurassic extensional fault-blocks
733 during the development of the northern North Sea. *Journal of the Geological Society*,
734 153(6), 931–944. <https://doi.org/10.1144/gsjgs.153.6.0931>
- 735 Fichler, C., Odinsen, T., Rueslåtten, H., Olesen, O., Vindstad, J. E., & Wienecke, S. (2011).
736 Crustal inhomogeneities in the Northern North Sea from potential field modeling:

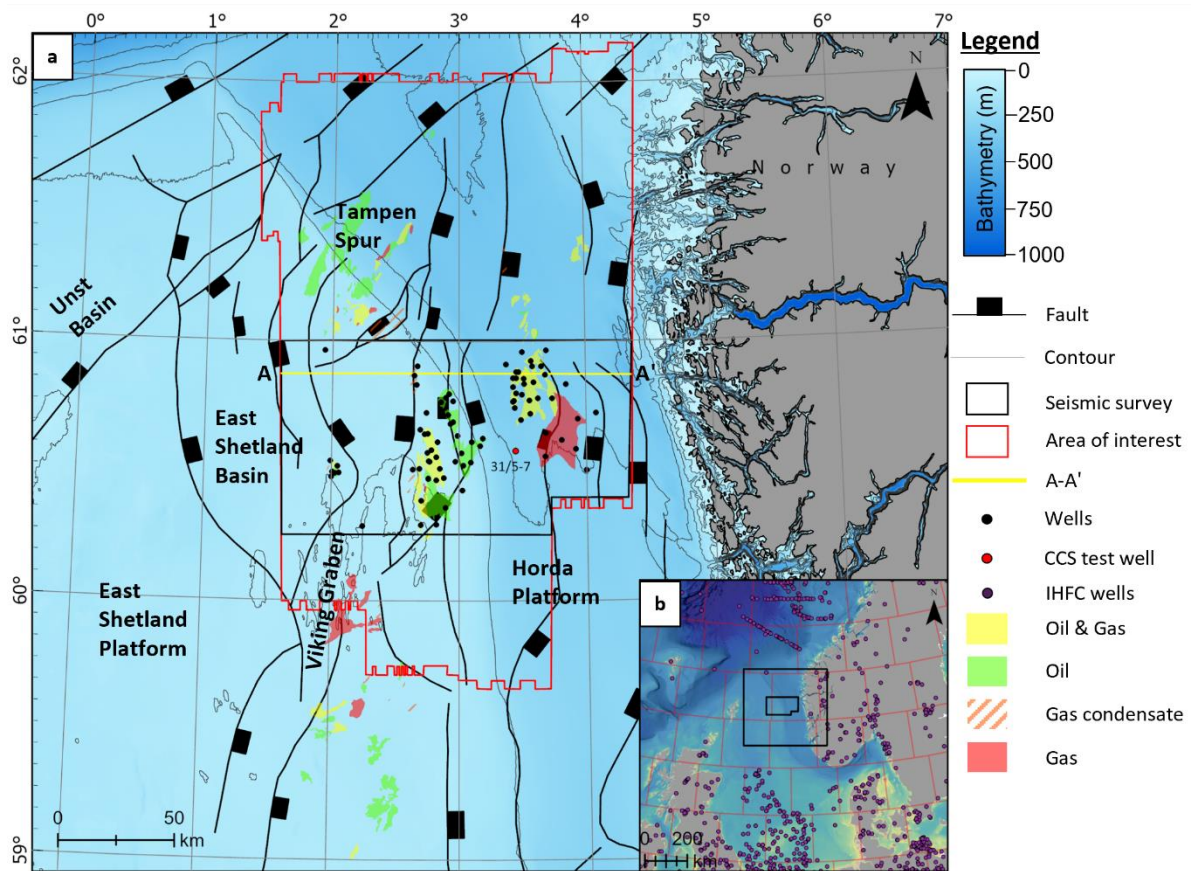
- 737 Inherited structure and serpentinites? *Tectonophysics*, 510(1–2), 172–185.
738 <https://doi.org/10.1016/j.tecto.2011.06.026>
- 739 Fossen, H., Pedersen, R. B., Bergh, S., & Andresen, A. (2008). Creation of a mountain chain. In
740 I. B. Ramberg, I. Bryhni, A. Nøttvedt, & K. Rangnes (Eds.), *The Making of a Land: geology*
741 *of Norway* (pp. 178–232). The Norwegian Geological Association.
- 742 Fuchs, S., & Balling, N. (2016). Improving the temperature predictions of subsurface thermal
743 models by using high-quality input data. Part 2: A case study from the Danish-German
744 border region. *Geothermics*, 64, 1–14.
745 <https://doi.org/10.1016/j.geothermics.2016.04.004>
- 746 Fuchs, S., & Förster, A. (2013). Well-log based prediction of thermal conductivity of
747 sedimentary successions: A case study from the north german basin. *Geophysical Journal*
748 *International*, 196(1), 291–311. <https://doi.org/10.1093/gji/ggt382>
- 749 Galson, D. A., Wilson, N. P., Schärli, U., & Rybach, L. (1987). A comparison of the divided-bar
750 and QTM methods of measuring thermal conductivity. *Geothermics*, 16(3), 215–226.
751 [https://doi.org/10.1016/0375-6505\(87\)90001-0](https://doi.org/10.1016/0375-6505(87)90001-0)
- 752 Gautier, D. L. (2005). *Kimmeridgian shales total petroleum system of the North Sea graben*
753 *province*. US Geological Survey.
- 754 Gegenhuber, N., & Schoen, J. (2012). New approaches for the relationship between
755 compressional wave velocity and thermal conductivity. *Journal of Applied Geophysics*,
756 76, 50–55. <https://doi.org/10.1016/j.jappgeo.2011.10.005>
- 757 Goff, J. C. (1983). Hydrocarbon generation and migration from Jurassic source rocks in the E
758 Shetland Basin and Viking Graben of the northern North Sea. *Journal - Geological Society*
759 *London*, 140(3), 445–474. <https://doi.org/10.1144/gsjgs.140.3.0445>
- 760 Gosnold, W., & Panda, B. (2002). *The Global Heat Flow Database of the International Heat*
761 *Flow Commission*. <https://doi.org/http://doi.org/10.17616/R3G305>
- 762 Grad, M., & Tiira, T. (2009). The Moho depth map of the European Plate. *Geophysical Journal*
763 *International*, 176(1), 279–292. <https://doi.org/10.1111/j.1365-246X.2008.03919.x>
- 764 Grevemeyer, I., & Villinger, H. (2001). Gas hydrate stability and the assessment of heat flow
765 through continental margins. *Geophysical Journal International*, 145, 647–660.
766 <https://doi.org/ISI:000169428800007>
- 767 Gu, Y., Rühaak, W., Bär, K., & Sass, I. (2017). Using seismic data to estimate the spatial
768 distribution of rock thermal conductivity at reservoir scale. *Geothermics*, 66, 61–72.
769 <https://doi.org/10.1016/j.geothermics.2016.11.007>
- 770 Haaland, H. J., Furnes, H., & Martinsen, O. J. (2000). Paleogene tuffaceous intervals, Grane
771 Field (Block 25/11), Norwegian North Sea: their depositional, petrographical,
772 geochemical character and regional implications. *Marine and Petroleum Geology*, 17(1),
773 101–118. [https://doi.org/10.1016/S0264-8172\(99\)00009-4](https://doi.org/10.1016/S0264-8172(99)00009-4)
- 774 Harper, M. L. (1971). Approximate geothermal gradients in the North Sea basin. *Nature*,
775 230(5291), 235–236. <https://doi.org/10.1038/230235a0>

- 776 Hartmann, A. Ā., Rath, V., & Clauser, C. (2005). Thermal conductivity from core and well log
777 data. *International Journal of Rock Mechanics and Mining Sciences*, 42(7-8 SPEC. ISS.),
778 1042–1055. <https://doi.org/10.1016/j.ijrmms.2005.05.015>
- 779 Hasterok, D. (2010). *Thermal State of Continental and Oceanic Lithosphere*. The University of
780 Utah.
- 781 Hasterok, D., Chapman, D. S., & Davis, E. E. (2011). Oceanic heat flow: Implications for global
782 heat loss. *Earth and Planetary Science Letters*, 311(3–4), 386–395.
783 <https://doi.org/10.1016/j.epsl.2011.09.044>
- 784 Hazen, T. C. (1997). Bioremediation. In P. S. Amy & D. L. Haldeman (Eds.), *The Microbiology of*
785 *the Terrestrial Deep Subsurface* (pp. 247–266). CRC Press.
- 786 Hokstad, K., Tašárová, Z. A., Clark, S. A., Kyrkjebø, R., Duffaut, K., Fichler, C., & Wiik, T. (2017).
787 Radiogenic heat production in the crust from inversion of gravity and magnetic data.
788 *Norsk Geologisk Tidsskrift*, 97(3), 241–254. <https://doi.org/10.17850/njg97-3-04>
- 789 Horai, K. (1982). Thermal Conductivity of Sediments and Igneous Rocks Recovered during
790 Deep Sea Drilling Project Leg 60. In D. M. Hussong & S. Uyeda (Eds.), *Initial Reports of the*
791 *Deep Sea Drilling Project, 60* (Vol. 60, pp. 807–834). U.S. Government Printing Office.
792 <https://doi.org/10.2973/dsdp.proc.60.149.1982>
- 793 Houbolt, J. J. H. C., & Wells, P. R. A. (1980). Estimation of Heat Flow in Oil Wells Based on
794 Relation Between Heat Conductivity and Sound Velocity. *AAPG Bulletin*, 65(7), 1360–
795 1361.
- 796 Jones, I. F. (2018). *Velocities, Imaging, and Waveform Inversion – The evolution of*
797 *characterizing the Earth’s subsurface*. EAGE Publications.
- 798 Jorand, R., Clauser, C., Marquart, G., & Pechinig, R. (2015). Statistically reliable petrophysical
799 properties of potential reservoir rocks for geothermal energy use and their relation to
800 lithostratigraphy and rock composition: The NE Rhenish Massif and the Lower Rhine
801 Embayment (Germany). *Geothermics*, 53, 413–428.
802 <https://doi.org/10.1016/j.geothermics.2014.08.008>
- 803 Justwan, H., Meisingset, I., Dahl, B., & Isaksen, G. H. (2006). Geothermal history and
804 petroleum generation in the Norwegian South Viking Graben revealed by pseudo-3D
805 basin modelling. *Marine and Petroleum Geology*, 23(8), 791–819.
806 <https://doi.org/10.1016/j.marpetgeo.2006.07.001>
- 807 Kubala, M., Bastow, M., Thompson, S., Scotchman, I., & Oygard, K. (2003). Geothermal
808 regime, petroleum generation and migration. In D Evans, C. Graham, A. Armour, & P.
809 Bathurst (Eds.), *The Millenium Atlas: Petroleum Geology of the Central and Northern*
810 *North Sea* (pp. 285–315). The Geological Society of London.
- 811 Landrø, M., Solheim, O. A., Hilde, E., Ekren, B. O., & Strønen, L. K. (1999). The Gullfaks 4D
812 seismic study. *Petroleum Geoscience*, 5(3), 213–226.
813 <https://doi.org/10.1144/petgeo.5.3.213>
- 814 Leadholm, R. H., Ho, T. T. Y., & Sahai, S. K. (1985). Heat flow, geothermal gradients and
815 maturation modelling on the Norwegian continental shelf using computer methods. In
816 *Petroleum Geochemistry in Exploration of the Norwegian Shelf* (pp. 131–143). Springer

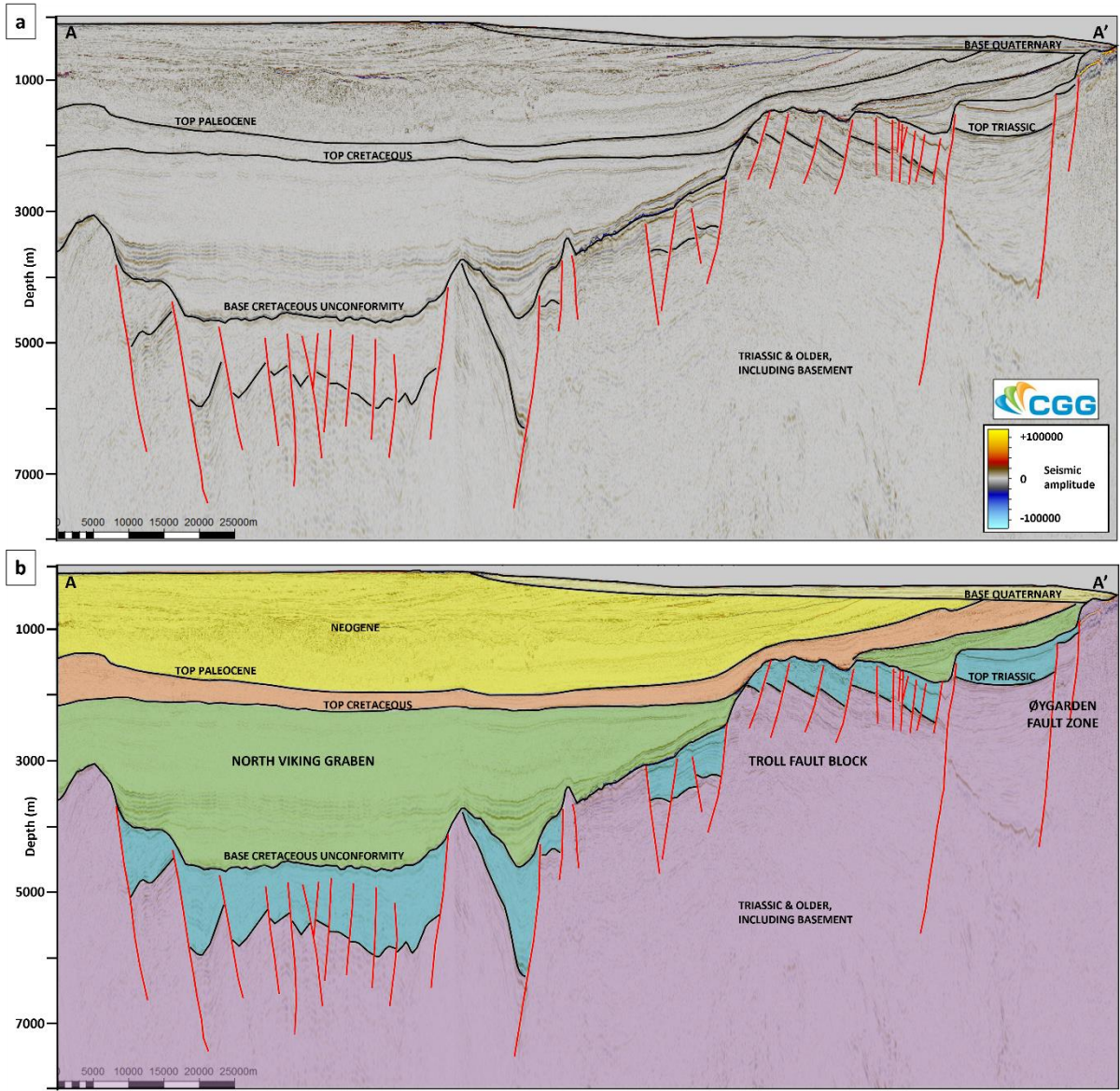
- 817 Netherlands. https://doi.org/10.1007/978-94-009-4199-1_9
- 818 Lee, M. W. (2003). Elastic properties of overpressured and unconsolidated sediments. In *U.S.*
819 *Geological Survey Bulletin* (Vol. 2214). <https://pubs.er.usgs.gov/publication/b2214>
- 820 Licciardi, A., England, R. W., Piana Agostinetti, N., & Gallagher, K. (2020). Moho depth of the
821 British Isles: a probabilistic perspective. *Geophysical Journal International*, 221(2), 1384–
822 1401. <https://doi.org/10.1093/gji/ggaa021>
- 823 Lister, C. R. B. (1972). On the Thermal Balance of a Mid-Ocean Ridge. *Geophysical Journal*
824 *International*, 26(5), 515–535. <https://doi.org/10.1111/j.1365-246X.1972.tb05766.x>
- 825 Locarnini, R. A., Mishonov, A. V, Antonov, J. I., Boyer, T. P., Garcia, H. E., Baranova, O. K.,
826 Zweng, M. M., Paver, C. R., Reagan, J. R., Johnson, D. R., Hamilton, M., & Seidov, D.
827 (2013). *WORLD OCEAN ATLAS 2013: Temperature Volume 1* (Vol. 1, Issue NOAA Atlas
828 NESDID 81). <https://doi.org/10.7289/V55X26VD>
- 829 Løseth, H., Øygarden, B., Nygård, A., & Raulline, B. (2016). Reply to Discussion on ‘Late
830 Cenozoic geological evolution of the northern North Sea: development of a Miocene
831 unconformity reshaped by large-scale Pleistocene sand intrusion’, *Journal of the*
832 *Geological Society*, 170, 133–145 [Article]. *Journal of the Geological Society*, 173(2),
833 394–397. <https://doi.org/10.1144/jgs2015-104>
- 834 Løseth, H., Raulline, B., & Nygård, A. (2013). Late Cenozoic geological evolution of the
835 northern North Sea: development of a Miocene unconformity reshaped by large-scale
836 Pleistocene sand intrusion. *Journal of the Geological Society*, 170(1), 133–145.
837 <https://doi.org/10.1144/jgs2011-165>
- 838 Lucazeau, F. (2019). Analysis and Mapping of an Updated Terrestrial Heat Flow Data Set.
839 *Geochemistry, Geophysics, Geosystems*, 20(8), 4001–4024.
840 <https://doi.org/10.1029/2019GC008389>
- 841 Lucazeau, F., & Le Douaran, S. (1985). The blanketing effect of sediments in basins formed by
842 extension: a numerical model. Application to the Gulf of Lion and Viking graben. *Earth*
843 *and Planetary Science Letters*, 74(1), 92–102. [https://doi.org/10.1016/0012-](https://doi.org/10.1016/0012-821X(85)90169-4)
844 [821X\(85\)90169-4](https://doi.org/10.1016/0012-821X(85)90169-4)
- 845 Lucazeau, Francis, Brigaud, F., & Bouroulllec, J. L. (2004). High-resolution heat flow density in
846 the lower Congo basin. *Geochemistry, Geophysics, Geosystems*, 5(3), Q03001.
847 <https://doi.org/10.1029/2003GC000644>
- 848 Mareschal, J., & Jaupart, C. (2013). Radiogenic heat production, thermal regime and evolution
849 of continental crust. *Tectonophysics*, 609, 524–534.
850 <https://doi.org/10.1016/j.tecto.2012.12.001>
- 851 Mavko, G., Mukerji, T., & Dvorkin, J. (2009). *The rock physics handbook : tools for seismic*
852 *analysis of porous media* (T. Mukerji 1965-, J. Dvorkin 1953-, T. Mukerji 1965- author, &
853 J. Dvorkin 1953- author (eds.); 2nd ed.). Cambridge : Cambridge University Press.
- 854 Meert, J. G., & Torsvik, T. H. (2003). The making and unmaking of a supercontinent: Rodinia
855 revisited. *Tectonophysics*, 375(1–4), 261–288. [https://doi.org/10.1016/S0040-](https://doi.org/10.1016/S0040-1951(03)00342-1)
856 [1951\(03\)00342-1](https://doi.org/10.1016/S0040-1951(03)00342-1)

- 857 Mielke, P., Bär, K., & Sass, I. (2017). Determining the relationship of thermal conductivity and
858 compressional wave velocity of common rock types as a basis for reservoir
859 characterization. *Journal of Applied Geophysics*, 140, 135–144.
860 <https://doi.org/10.1016/j.jappgeo.2017.04.002>
- 861 Nadeau, P. H. (2011). Earth's energy "Golden Zone": a synthesis from mineralogical research.
862 *Clay Minerals*, 46(1), 1–24. <https://doi.org/10.1180/claymin.2011.046.1.1>
- 863 Nottvedt, A., Gabrielsen, R. H., & Steel, R. J. (1995). Tectonostratigraphy and sedimentary
864 architecture of rift basins, with reference to the northern North Sea. *Marine and*
865 *Petroleum Geology*, 12(8), 881–901. [https://doi.org/10.1016/0264-8172\(95\)98853-W](https://doi.org/10.1016/0264-8172(95)98853-W)
- 866 Philip, G. M., & Watson, D. F. (1982). A Precise Method for Determining Contoured Surfaces.
867 *The APPEA Journal*, 22(1), 205–212. <https://doi.org/doi.org/10.1071/AJ81016>
- 868 Pimienta, L., Klitzsch, N., & Clauser, C. (2018). Comparison of thermal and elastic properties
869 of sandstones: Experiments and theoretical insights. *Geothermics*, 76(June), 60–73.
870 <https://doi.org/10.1016/j.geothermics.2018.06.005>
- 871 Pollack, H. N., Hurter, S. J., & Johnson, J. R. (1993). Heat flow from the Earth's interior: Analysis
872 of the global data set. *Reviews of Geophysics*, 31(3), 267.
873 <https://doi.org/10.1029/93RG01249>
- 874 Popov, Y. A., Pribnow, D. F. C., Sass, J. H., Williams, C. F., & Burkhardt, H. (1999).
875 Characterization of rock thermal conductivity by high-resolution optical scanning.
876 *Geothermics*, 28(2), 253–276. [https://doi.org/10.1016/S0375-6505\(99\)00007-3](https://doi.org/10.1016/S0375-6505(99)00007-3)
- 877 Popov, Y., Tertychnyi, V., Romushkevich, R., Korobkov, D., & Pohl, J. (2003). Interrelations
878 Between Thermal Conductivity and Other Physical Properties of Rocks: Experimental
879 Data. *Pure and Applied Geophysics*, 160(5), 1137–1161.
880 <https://doi.org/10.1007/PL00012565>
- 881 Posamentier, H. W. (2004). Seismic Geomorphology: Imaging Elements of Depositional
882 Systems from Shelf to Deep Basin Using 3D Seismic Data: Implications for Exploration
883 and Development. *Geological Society, London, Memoirs*, 29(1), 11–24.
884 <https://doi.org/10.1144/GSL.MEM.2004.029.01.02>
- 885 Prada, M., Lavoué, F., Saqab, M. M., O'Reilly, B. M., Lebedev, S., Walsh, J. J., & Childs, C.
886 (2019). Across-axis variations in petrophysical properties of the North Porcupine Basin,
887 offshore Ireland: New insights from long-streamer traveltime tomography. *Basin*
888 *Research*, 31(1), 59–76. <https://doi.org/10.1111/bre.12308>
- 889 Pribnow, D. F. C., Kinoshita, M., & Stein, C. . (2000). Thermal data collection and heat flow
890 recalculations for ODP Legs 101-180. In *Institute for Joint Geoscientific Research*.
891 <http://www-odp.tamu.edu/publications/heatflow/>
- 892 Purvis, S., Caughtry, N., Mann, J., & Rumyantseva, A. (2018). *Northern Viking Graben Well*
893 *Study* (Issue 10592).
- 894 Rajaram, M., Anand, S. P., Hemant, K., & Purucker, M. E. (2009). Curie isotherm map of Indian
895 subcontinent from satellite and aeromagnetic data. *Earth and Planetary Science Letters*,
896 281(3–4), 147–158. <https://doi.org/10.1016/j.epsl.2009.02.013>

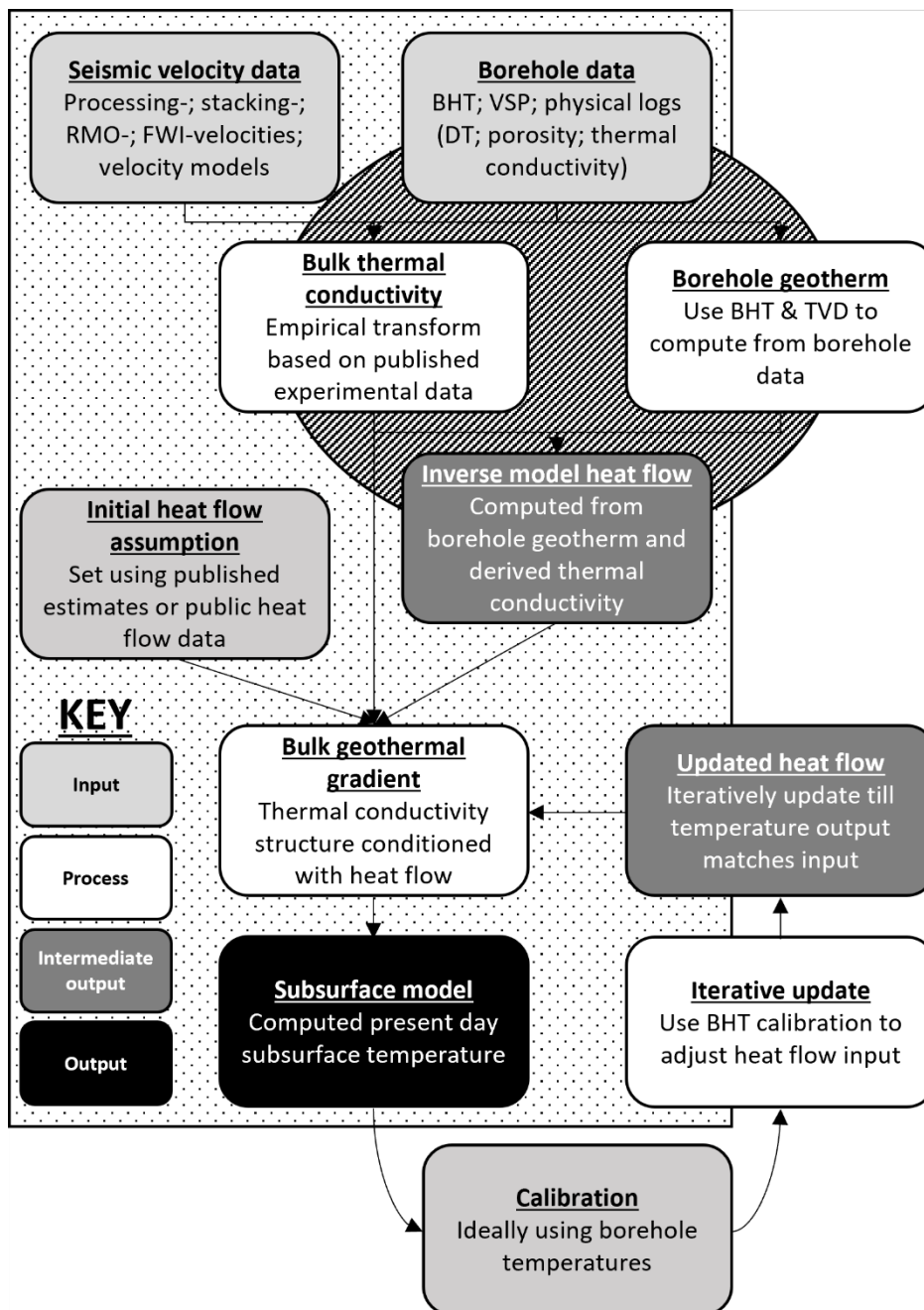
- 897 Ritter, U., Zielinski, G. W., Weiss, H. M., Zielinski, R. L. B., & Sættem, J. (2004). Heat flow in the
898 Vøring Basin, Mid-Norwegian Shelf. *Petroleum Geoscience*, 10(4), 353–365.
899 <https://doi.org/10.1144/1354-079303-616>
- 900 Rüpke, L. H., Schmalholz, S. M., Schmid, D. W., & Podladchikov, Y. Y. (2008). Automated
901 thermotectonostratigraphic basin reconstruction: Viking Graben case study. *AAPG*
902 *Bulletin*, 92(3), 309–326. <https://doi.org/10.1306/11140707009>
- 903 Sarkar, A. D. (2020). *Reflection Seismic Thermometry* [University of Manchester].
904 <https://doi.org/10.31237/osf.io/fk7pb>
- 905 Sarkar, A. D., & Huuse, M. (2018). Subsurface Temperature Prediction From Seismic
906 Measurements: A 3-D Seismic Case Study From The Lüderitz Basin, Offshore Namibia.
907 *AAPG International Conference and Exhibition*.
908 <https://www.searchanddiscovery.com/abstracts/html/2018/ice2018/abstracts/296533>
909 7.html
- 910 Sarkar, A. D., & Huuse, M. (2021). Thermal regime of Blake Ridge using seismic and borehole
911 data. *Geochemistry, Geophysics, Geosystems*, (in prep.), 1–41.
912 <https://doi.org/doi.org/10.1002/essoar.10506898.1>
- 913 Schön, J. H. (2015a). Appendix. In *Physical Properties of Rocks* (Vol. 65, Issue 1995, pp. 445–
914 453). <https://doi.org/10.1016/B978-0-08-100404-3.10000-9>
- 915 Schön, J. H. (2015b). Thermal Properties. In *Developments in Petroleum Science* (Vol. 65, pp.
916 369–414). <https://doi.org/10.1016/B978-0-08-100404-3.00009-3>
- 917 The GEBCO_2019 Grid - a continuous terrain model of the global oceans and land. (2019). In
918 *GEBCO Bathymetric Compilation Group*. British Oceanographic Data Centre, National
919 Oceanography Centre, NERC, UK. <https://doi.org/10.5285/836f016a-33be-6ddc-e053->
920 6c86abc0788e
- 921 Velde, B. (1996). Compaction trends of clay-rich deep sea sediments. *Marine Geology*, 133(3–
922 4), 193–201. [https://doi.org/10.1016/0025-3227\(96\)00020-5](https://doi.org/10.1016/0025-3227(96)00020-5)
- 923 Wangen, M. (1995). The blanketing effect in sedimentary basins. *Basin Research*, 7(4), 283–
924 298. <https://doi.org/10.1111/j.1365-2117.1995.tb00118.x>
- 925 Warner, M., Ratcliffe, A., Nangoo, T., Morgan, J., Umpleby, A., Shah, N., Vinje, V., Štekl, I.,
926 Guasch, L., Win, C., Conroy, G., & Bertrand, A. (2013). Anisotropic 3D full-waveform
927 inversion. *Geophysics*, 78(2), R59–R80. <https://doi.org/10.1190/geo2012-0338.1>
- 928 Watson, D. F., & Philip, G. M. (1985). A refinement of inverse distance weighted interpolation.
929 *Geoprocessing*, 2(4), 315–327.
- 930 Zamora, M., Vo-Thanh, D., Bienfait, G., & Poirier, J. P. (1993). An empirical relationship
931 between thermal conductivity and elastic wave velocities in sandstone. *Geophysical*
932 *Research Letters*, 20(16), 1679–1682. <https://doi.org/10.1029/92GL02460>
- 933 Ziegler, P. A. (1992). North Sea rift system. *Tectonophysics*, 208(1–3), 55–75.
934 [https://doi.org/10.1016/0040-1951\(92\)90336-5](https://doi.org/10.1016/0040-1951(92)90336-5)
- 935



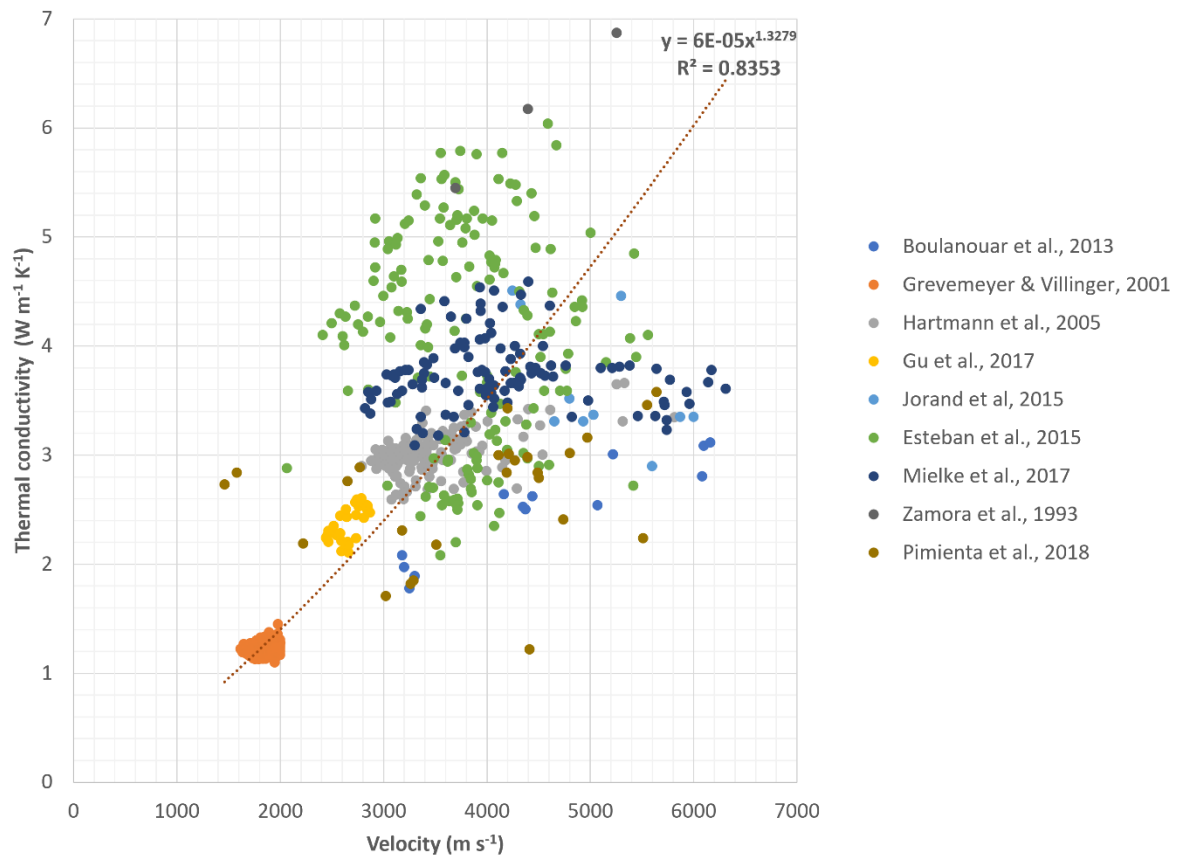
937
 938 *Figure 1: (a) Study area in the northern North Sea outlining the extent of the CGG NVG*
 939 *survey (displayed in red) offshore the Norwegian continental shelf with structural features*
 940 *displayed from (Færseth, 1996). Transect A-A' based on NVG type section (Copestake et al.,*
 941 *2003). Exploration wells displayed are used for calibration. Northern Lights CCS test well*
 942 *31/5-7 also displayed (red circle) (between Brage and Troll fields). Bathymetry from*
 943 *Generalised Bathymetric Chart of the Oceans (GEBCO) (Becker et al., 2009; "The*
 944 *GEBCO_2019 Grid - a continuous terrain model of the global oceans and land.," 2019). (b)*
 945 *Existing heatflow data from the IHFC (purple points) shows a scarcity of data in the model*
 946 *area (Gosnold & Panda, 2002). Relying on published heatflow grids such as the Davies (2013)*
 947 *shown above (red grid) demonstrates the coarseness of the data when compared to the*
 948 *scale of the model area (Davies, 2013).*
 949



950
 951 *Figure 2: (a) East West transect A-A' displaying reflection seismic data, annotated with*
 952 *major chronostratigraphic surfaces and structures of note. (b) Overlay of major intervals*
 953 *highlighting the geometry of the NVG in the west of the model area, with tilted fault blocks*
 954 *apparent. The study area is bounded to the west by the East Shetland Basin, with the eastern*
 955 *limits coinciding with the Horda platform. Adapted from (Copestake et al., 2003).*
 956



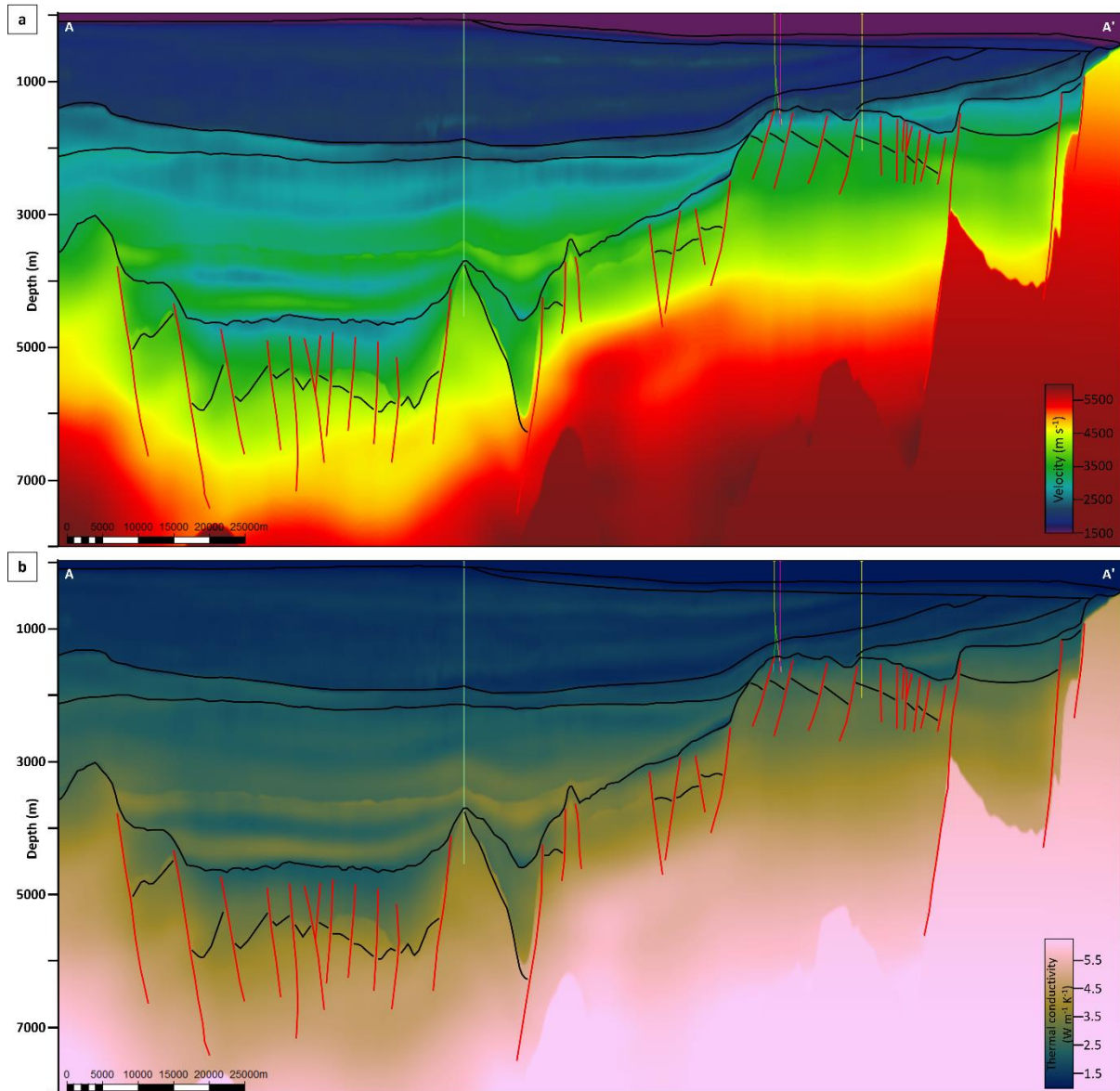
957
 958 *Figure 3: Model building workflow displayed in terms of input, processing steps and*
 959 *outputs/deliverables. There are two main pathways, a forward modelling pathway*
 960 *(demarcated with the dotted background polygon) where seismic data is used to simulate*
 961 *BHTs; and an inverse modelling pathway (demarcated with the hashed background polygon)*
 962 *where BHTs are used to determine the heatflow conditions needed for it. This allows for an*
 963 *iterative final forward modelling pathway utilising the derived heatflow to arrive at a*
 964 *subsurface temperature model representative of present-day conditions.*



966

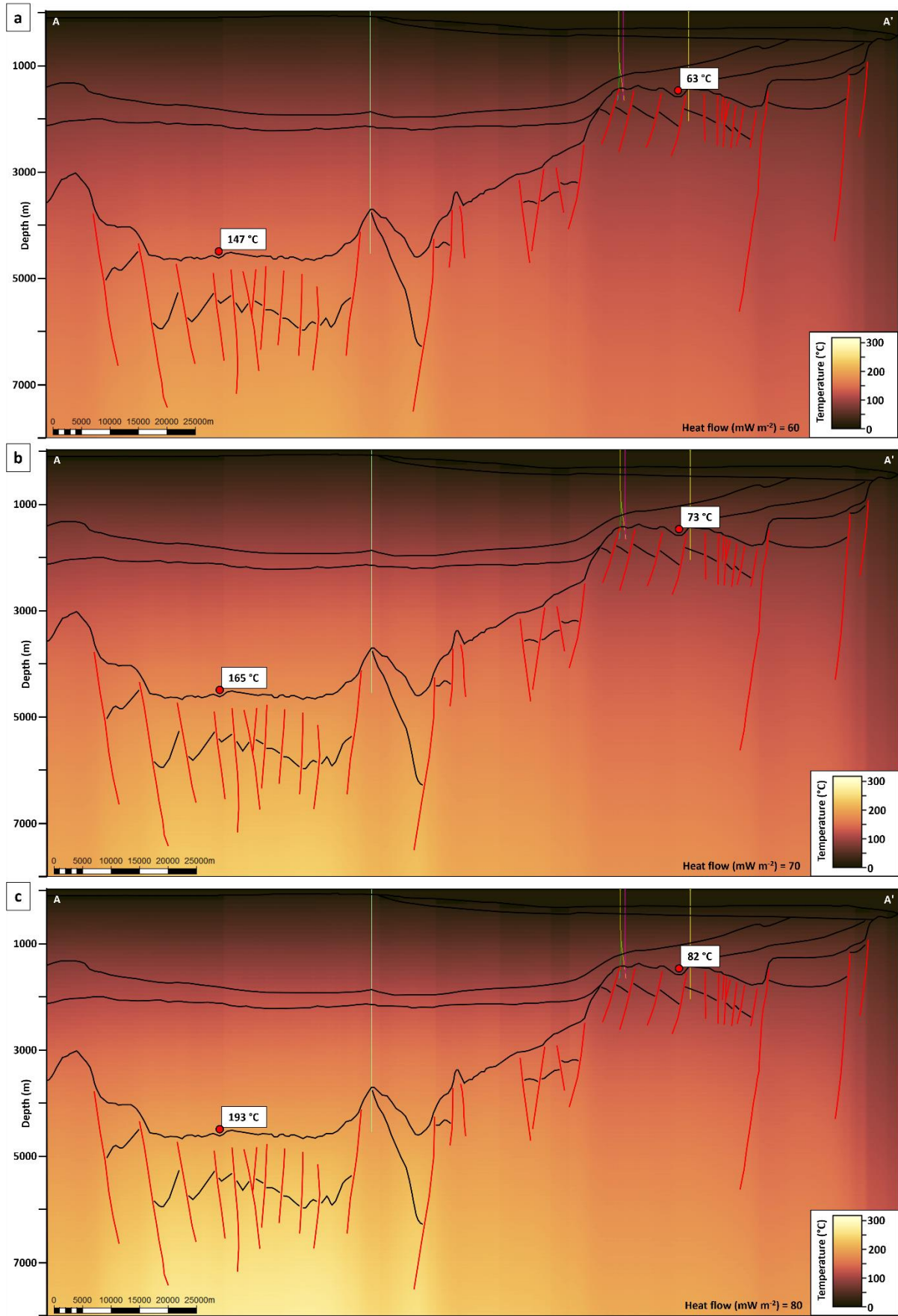
967 *Figure 4: Bulk shift transform from velocity to thermal conductivity derived from*
 968 *experimental data published in the literature. All points displayed are wet samples with*
 969 *laboratory measurements of both velocity and thermal conductivity having been done with*
 970 *similar tools. This is to both reflect the presence of fluids in the subsurface and to also reduce*
 971 *the variables between displayed data respectively.*

972



973
 974
 975
 976

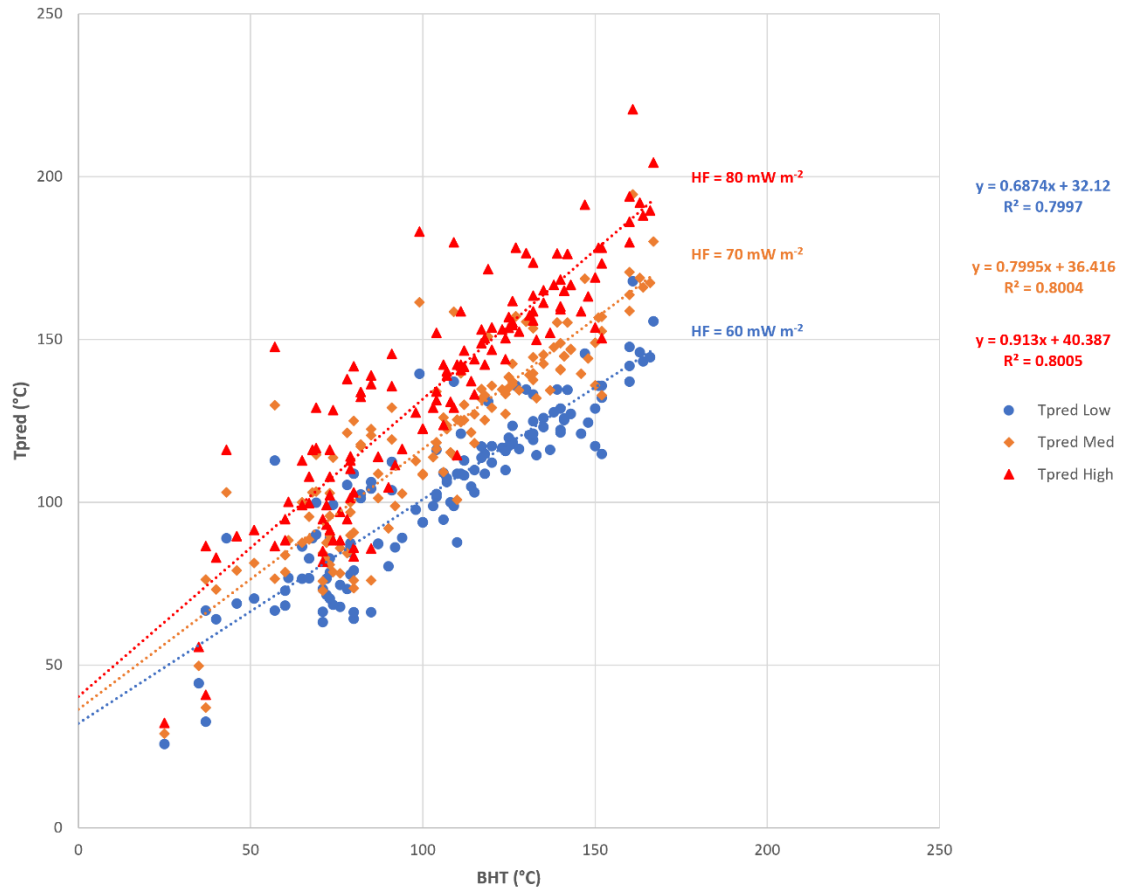
Figure 5: (a) Interval velocities with wells displayed. (b) Instantaneous thermal conductivity from interval velocities using scientific colour bar (Crameri et al., 2020).



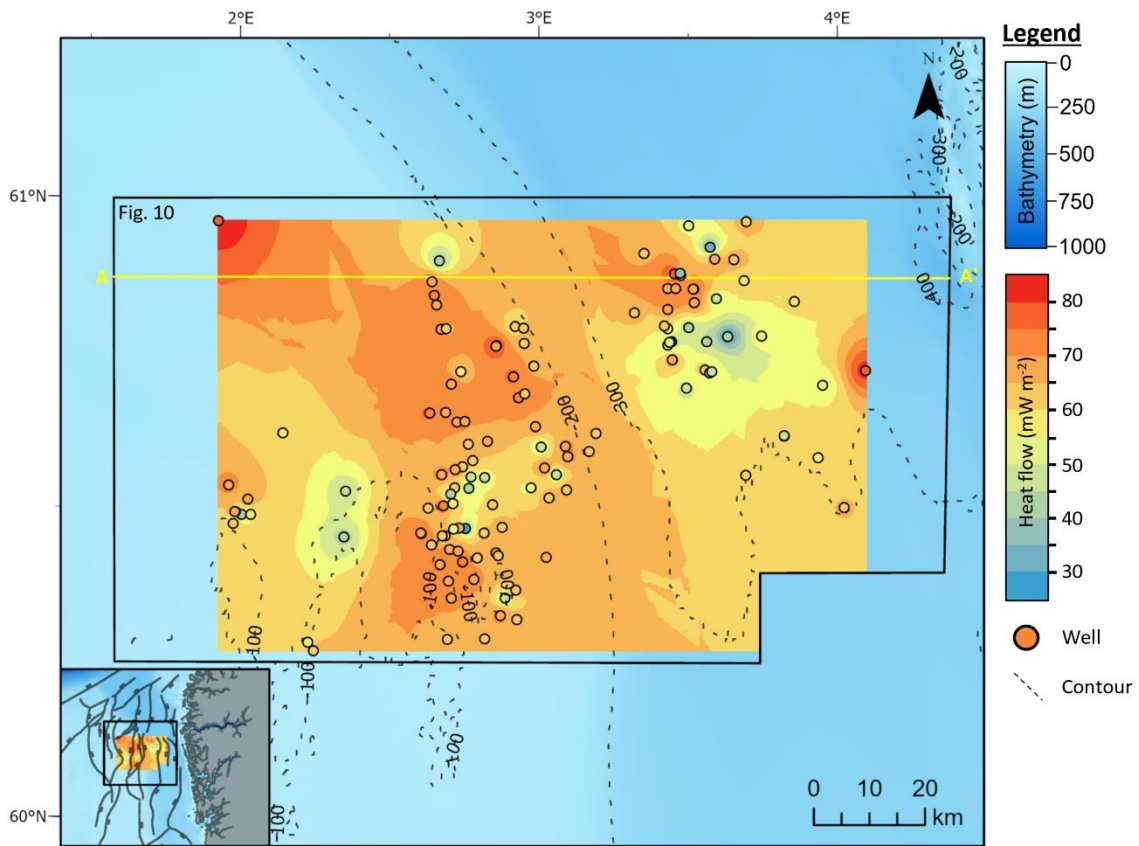
977
978
979

Figure 6: Forward modelling temperature prediction profiles with transect A-A' overlain for (a) low case (60 mW m^{-2}); (b) mid case (70 mW m^{-2}); & (c) high case (80 mW m^{-2}) heatflow

980 scenarios respectively. Temperature readings in the graben centre and on the graben flank
981 are shown for reference. Highest temperatures are observed in the heart of the graben.
982 Block like appearance is an artefact of the dimensions of the individual voxels comprising the
983 thermal model pillar grid used to represent the subsurface.
984

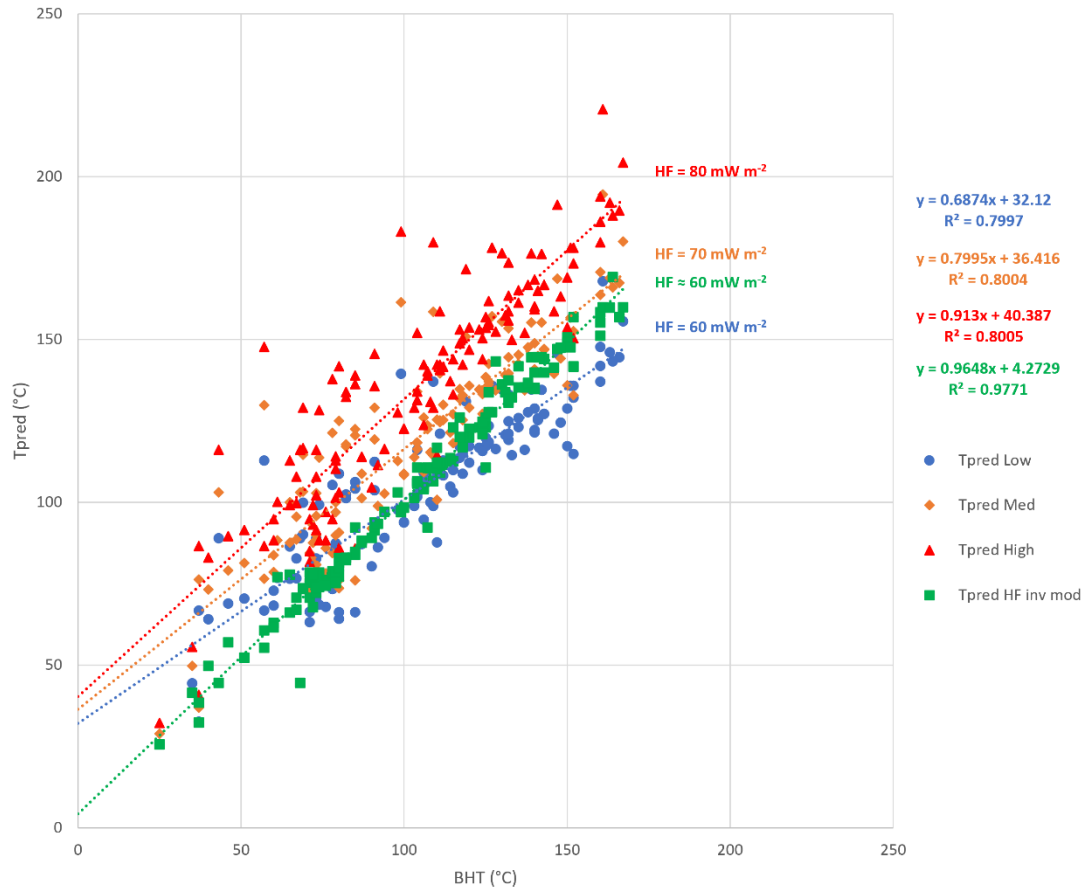


985
986 *Figure 7: Cross plot of BHT against predicted temperatures (Tpred) for each of the three*
987 *forward modelling starting conditions for heatflow (low; mid and high case corresponding to*
988 *60; 70 and 80 mW m⁻² respectively). With increasing input heatflow a corresponding*
989 *increase is seen in the gradient of the regression line through that set of points.*
990



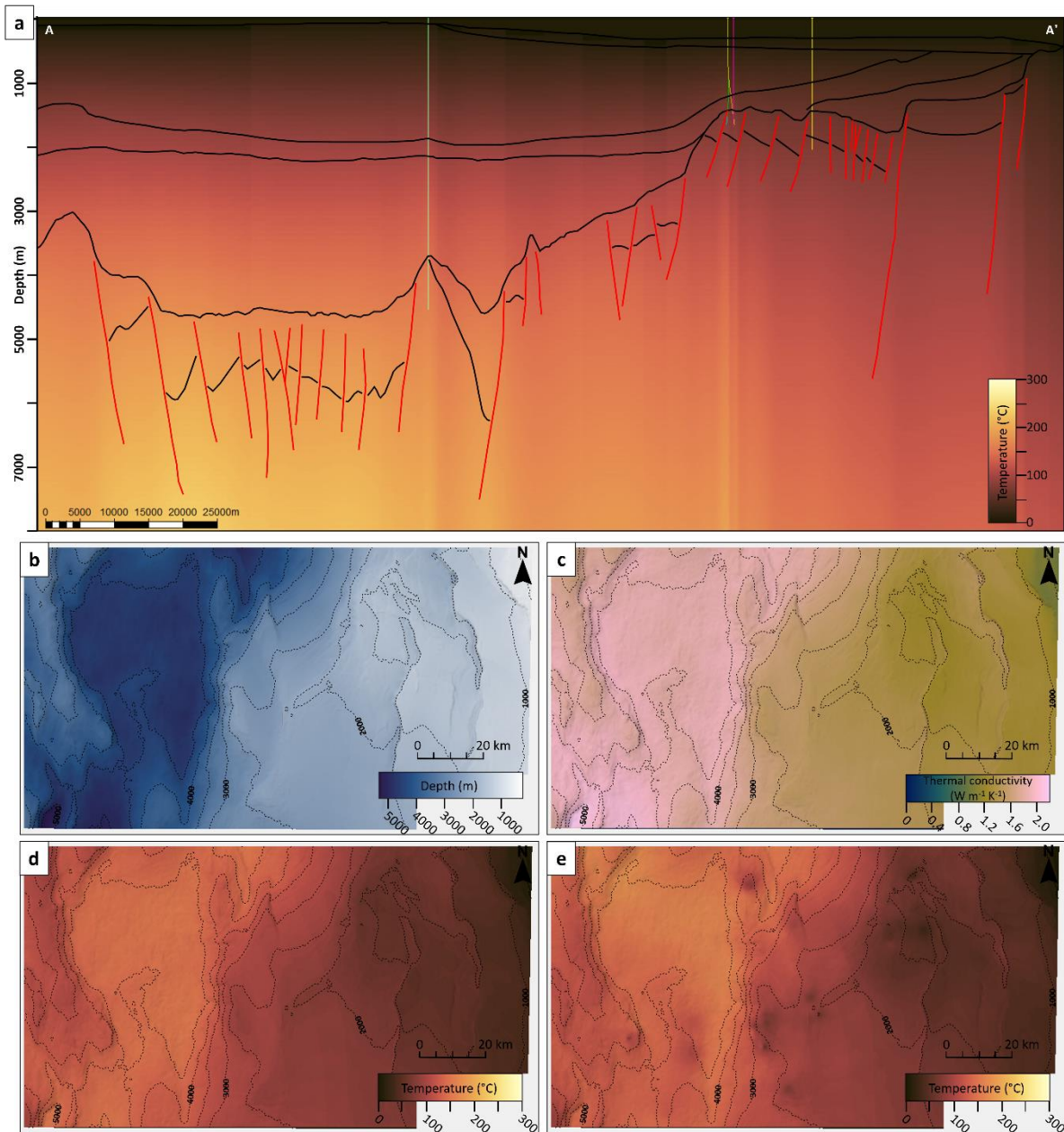
991
 992
 993
 994
 995

Figure 8: Inverse modelling of heatflow at each well location from BHT and TVD. This data is used to interpolate heatflow across the model area. Interpolated heatflow shows lateral variability at much higher resolution than published global grids.



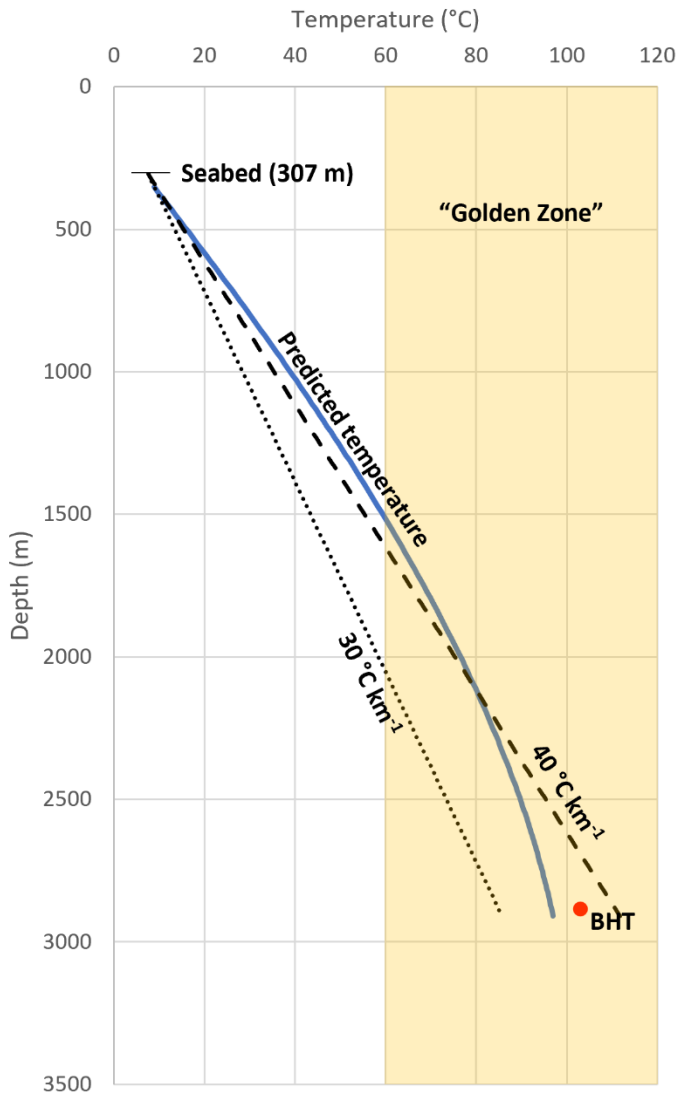
996
 997
 998
 999
 1000
 1001
 1002

Figure 9: Cross plot of BHT against predicted temperatures (Tpred) with model results using inverse modelling of heatflow across the area displayed (green squares). R-squared for this regression suggests a good statistical fit, the results having a gradient verging on 1:1 as would be expected for results best reflecting the actual subsurface temperature conditions. Furthermore, the spread of points is much narrower for this modelling outcome.



1003
 1004
 1005
 1006
 1007
 1008
 1009
 1010
 1011
 1012
 1013

Figure 10: (a) Final temperature model produced using inverse modelling of heatflow overlain on transect A-A' (with well paths and BCU displayed). (b) BCU in depth with 500 m interval contours shown. (c) RMS amplitude extraction of derived thermal conductivity at BCU. Where BCU is interpreted to shallow towards the northeast, there are correspondingly low conductivities that reflect Quaternary sediments in this region instead. (d) Low case prediction of temperature along BCU. (e) Final temperature prediction using inverse modelled heatflow along BCU. Comparing with (d) some differences are apparent. Bulls eye like temperature anomalies in the northeast are likely the translation of the interpolated heatflow (see Fig. 8).



1014

1015 *Figure 11: Modelled subsurface temperature at well 31/5-7 (see Fig. 1) as part of the*
 1016 *Northern Lights CCS project. “Golden zone” for sandstone reservoirs is also displayed for*
 1017 *context. BHT displayed is from October 2020 data release of preliminary results, indicating*
 1018 *that prediction is in close agreement with what was discovered downhole (prediction is*
 1019 *offset by 6 °C to reported BHT). Also shown are the temperature profiles taken from seabed*
 1020 *assuming a constant linear geothermal gradient. Typically used geothermal gradients in*
 1021 *basin modelling are 30 °C km⁻¹ (dotted line) and 40 °C km⁻¹ (dashed line). These are displayed*
 1022 *to show how much subsurface temperature predictions may vary using standard processes,*
 1023 *particularly at bottom hole (up to ±13 °C).*

1024

1025 A.1 Appendix

Source	Geothermal gradient (°C/km)	Heatflow (mW m ⁻²)
(Harper, 1971)	29.7	49.8 – 62.0
(Evans, 1977)		63
(Brigaud et al., 1992)	31.8 – 36.3	50 – 65
(Leadholm et al., 1985)	30 – 35	58.6 – 67
(Justwan et al., 2006)		52.3
(Cornford, 1998)		60 – 82
(Lucazeau & Le Douaran, 1985)		65
(Goff, 1983)	32	57 – 65
(Rüpke et al., 2008)	30 – 40	
(Ritter et al., 2004)		65

1026 *Table A.1: Some examples of reported geothermal gradient and heatflow for the NVG and*
 1027 *surrounding basins from the literature.*

1028

1029